

RESEARCH ARTICLE

10.1002/2015JD023941

Special Section:

Deep Convective Clouds and Chemistry 2012 Studies (DC3)

Key Points:

- Moles of NO_x produced per lightning flash are reported for six thunderstorms
- Two calculation methods are evaluated and compared using a common data set
- Results are compared with those for other storms over the U.S. Great Plains

Supporting Information:

- Texts S1–S5, Figures S1–S8, and Table S1

Correspondence to:

I. B. Pollack,
ipollack@rams.colostate.edu

Citation:

Pollack, I. B., et al. (2016), Airborne quantification of upper tropospheric NO_x production from lightning in deep convective storms over the United States Great Plains, *J. Geophys. Res. Atmos.*, 121, 2002–2028, doi:10.1002/2015JD023941.

Received 14 JUL 2015

Accepted 27 JAN 2016

Accepted article online 29 JAN 2016

Published online 27 FEB 2016

Airborne quantification of upper tropospheric NO_x production from lightning in deep convective storms over the United States Great Plains

I. B. Pollack¹, C. R. Homeyer², T. B. Ryerson³, K. C. Aikin^{3,4}, J. Peischl^{3,4}, E. C. Apel⁵, T. Campos⁵, F. Flocke⁵, R. S. Hornbrook⁵, D. J. Knapp⁵, D. D. Montzka⁵, A. J. Weinheimer⁵, D. Riemer⁶, G. Diskin⁷, G. Sachse⁸, T. Mikoviny⁹, A. Wisthaler¹⁰, E. Bruning¹¹, D. MacGorman¹², K. A. Cummings¹³, K. E. Pickering¹⁴, H. Huntrieser¹⁵, M. Lichtenstern¹⁵, H. Schlager¹⁵, and M. C. Barth⁵

¹Atmospheric Science Department, Colorado State University, Fort Collins, Colorado, USA, ²School of Meteorology, University of Oklahoma, Norman, Oklahoma, USA, ³Chemical Sciences Division, Earth System Research Laboratory, National Oceanic and Atmospheric Administration, Boulder, Colorado, USA, ⁴Cooperative Institute for Research in Environmental Sciences, University of Colorado Boulder, Boulder, Colorado, USA, ⁵Atmospheric Chemistry Division, National Center for Atmospheric Research, Boulder, Colorado, USA, ⁶Rosenstiel School of Marine and Atmospheric Science, University of Miami, Miami, Florida, USA, ⁷Oak Ridge Associated Universities (ORAU), Oak Ridge, Tennessee, USA, ⁸NASA Langley Research Center, Hampton, Virginia, USA, ⁹Department of Chemistry, University of Oslo, Oslo, Norway, ¹⁰Institut für Ionenphysik und Angewandte Physik, Innsbruck, Austria, ¹¹Department of Geosciences, Texas Tech University, Lubbock, Texas, USA, ¹²NOAA National Severe Storms Laboratory, Norman, Oklahoma, USA, ¹³Department of Atmospheric and Oceanic Science, University of Maryland, College Park, Maryland, USA, ¹⁴Atmospheric Chemistry and Dynamics Laboratory, NASA Goddard Space Flight Center, Greenbelt, Maryland, USA, ¹⁵Institut für Physik der Atmosphäre, Deutsches Zentrum für Luft- und Raumfahrt (DLR), Oberpfaffenhofen, Germany

Abstract The reported range for global production of nitrogen oxides (NO_x = NO + NO₂) by lightning remains large (e.g., 32 to 664 mol NO_x flash⁻¹), despite incorporating results from over 30 individual laboratory, theoretical, and field studies since the 1970s. Airborne and ground-based observations from the Deep Convective Clouds and Chemistry experiment in May and June 2012 provide a new data set for calculating moles of NO_x produced per lightning flash, $P(\text{NO}_x)$, in thunderstorms over the United States Great Plains. This analysis utilizes a combination of in situ observations of storm inflow and outflow from three instrumented aircraft, three-dimensional spatial information from ground-based radars and satellite observations, and spatial and temporal information for intracloud and cloud-to-ground lightning flashes from ground-based lightning mapping arrays. Evaluation of two analysis methods (e.g., a volume-based approach and a flux-based approach) for converting enhancements in lightning-produced NO_x from volume-based mixing ratios to moles NO_x flash⁻¹ suggests that both methods equally approximate $P(\text{NO}_x)$ for storms with elongated anvils, while the volume-based approach better approximates $P(\text{NO}_x)$ for storms with circular-shaped anvils. Results from the more robust volume-based approach for three storms sampled over Oklahoma and Colorado during DC3 suggest a range of 142 to 291 (average of 194) moles NO_x flash⁻¹ (or 117–332 mol NO_x flash⁻¹ including uncertainties). Although not vastly different from the previously reported range for storms occurring in the Great Plains (e.g., 21–465 mol NO_x flash⁻¹), results from this analysis of DC3 storms offer more constrained upper and lower limits for $P(\text{NO}_x)$ in this geographical region.

1. Introduction

Production of nitric oxide (NO) from lightning is a significant contributor to upper tropospheric nitrogen oxide (NO_x = NO + NO₂) concentrations. Lightning has sufficient energy to heat air in the vicinity of the discharge channel to temperatures as high as 30,000 K leading to dissociation of molecular nitrogen (N₂) and oxygen (O₂) [Chameides et al., 1977]. NO production results from recombination of the molecular and atomic counterparts via (R1)–(R3) (e.g., the extended Zel'dovich mechanism) [Chameides et al., 1977; Chameides, 1979; Stark et al., 1996; Wang et al., 1998].



Production of nitrogen dioxide (NO₂) results from reaction of lightning-produced NO with ozone (O₃) in the surrounding air via reaction (R4).



Although most of the oxidized nitrogen in the atmosphere is due to anthropogenic emissions of NO_x, lightning-produced NO_x (LNO_x) may dominate in some regions. Anthropogenic emissions of NO_x are estimated to be 28 Tg N yr⁻¹ [Reis *et al.*, 2009], with the highest contribution from energy production and transportation. Other sources of NO_x contribute an additional 16 Tg N yr⁻¹, with 5 ± 3 Tg N yr⁻¹ attributed to lightning [Schumann and Huntrieser, 2007] and the remainder from soils and biomass burning [Martin *et al.*, 2003]. Excluding the contribution of NO_x from stratosphere-troposphere exchange, these estimates suggest that NO_x production from lightning may contribute as much as 11% to the total atmospheric NO_x emissions. This natural contribution from lightning is rather significant when compared to the fraction of anthropogenic total reactive nitrogen (NO_y) transported from the planetary boundary layer to the upper troposphere (e.g., 3 to 15%) [Li *et al.*, 2004; Parrish *et al.*, 2004; Stohl *et al.*, 2002] and the amount of NO_x directly emitted into the upper troposphere by aircraft (e.g., 0.44 Tg N yr⁻¹) [Lamarque *et al.*, 1996]. LNO_x production in the upper troposphere may also be more important than the 11% implies owing to longer chemical lifetimes for NO and NO_x at high altitudes and where it is geographically introduced [Barth *et al.*, 2012].

Accurate quantification of LNO_x production is important for understanding the role of this natural source in the upper troposphere and for improving the accuracy of global and regional air quality and climate models. Of specific concern is the oxidation of LNO_x to produce O₃ in the upper troposphere, where it acts as the main source of hydroxyl radicals and as a greenhouse gas. However, significant uncertainty in LNO_x production remains owing to uncertainties, and likely variability, in the amount of NO_x generated from each lightning flash. Schumann and Huntrieser [2007] compiled assessments of NO_x production flash⁻¹ from laboratory, theoretical, and field studies around the world between 1976 and 2007 and reported a global average of 250 mol NO_x flash⁻¹ with individual results ranging from 32 to 664 mol NO_x flash⁻¹.

Airborne and ground-based observations acquired during the Deep Convective Clouds and Chemistry (DC3) experiment in May and June 2012 [Barth *et al.*, 2015] provide a new data set for calculating a measurement-based range for NO_x production from lightning flashes in thunderstorms sampled over the United States Great Plains. Similar to previous airborne and ground-based field studies in this part of the U.S. [Dye *et al.*, 2000; Ridley *et al.*, 1996], the DC3 field study utilized multiple chemically instrumented aircraft for simultaneous, in situ sampling of trace gases and meteorological parameters in the inflow and outflow regions of convective systems, multiple ground-based radars, which provide a multidimensional time-evolved image of storm shape, size, development and progression, and ground-based lightning detection systems. In contrast, the DC3 data set affords the additional advantages of having a more complete suite of airborne chemistry measurements with improved instrumentation for high-sensitivity fast-time response measurements (including individual measurements of NO and NO₂) and the use of several ground-based lightning mapping arrays, which in comparison to other lightning detection networks have higher sensitivity and the capability to provide total (e.g., intracloud (IC) plus cloud-to-ground (CG)) flash counts, flash area, and flash length.

Our analysis starts with quantifying enhancements in NO_x arising from lightning-produced NO in the anvil outflow of several thunderstorms that developed during the DC3 experiment. Enhancements are quantified in terms of volume-based mixing ratios (e.g., parts per billion by volume) in section 3.1 and then converted to units of molecules m⁻³ for further analysis. In section 3.2, we apply and evaluate two methods for converting ambient molecules m⁻³ to production in units of molecules (or moles). The first is a volume-based approach, utilized by Ridley *et al.* [1996, 2004], that employs a calculated storm volume over which the LNO_x is equally distributed. The second is a flux-based approach, utilized by Chameides *et al.* [1987] and Huntrieser *et al.* [1998, 2002, 2008, 2009, 2011], that identifies a cross-sectional area through which a mass flux of NO_x is calculated in units of mol s⁻¹. Obtaining molecules (or moles) of NO_x produced flash⁻¹ for each storm then only requires knowing the number of lightning flashes that contributed to the observed NO_x and the time period over which those flashes occurred. As discussed in section 3.3, these flash parameters are determined from aircraft position and meteorological measurements in conjunction with the ground-based radar and lightning mapping data products simultaneously acquired during DC3. NO_x production flash⁻¹ is then calculated as

Table 1. Summary of DC3 Storms Selected for This Analysis

Date	Start Time ^a (UTC)	End Time ^b (UTC)	Sounding Time (UTC)	Sounding Location (longitude, latitude)	CAPE (m ² s ⁻²)	Max Updraft Velocity ^c (m s ⁻¹)	0–6 km Vertical Shear (m s ⁻¹)	Observations
<i>Oklahoma Region</i>								
19 May	21:20	01:16	00:11, 20 May	−98.835, 35.372	2,054	64	27	Double tropopause; storm dynamics induced stratospheric air wrapping around downwind edge of anvil cloud from above.
25 May	23:05	01:43	21:23	−99.439, 34.642	3,650	85	13	Isolated storm with motion in the downwind direction.
29 May	21:35	00:46	20:29	−98.341, 35.667	3,113	79	19	Isolated storm with motion in the downwind direction.
30 May ^d	21:35	00:24	22:19	−99.394, 34.073	2,216	67	25	Isolated storm with motion in the downwind direction.
16 June	19:20	00:21	21:21	−97.964, 35.088	3,049	78	16	Isolated storm with little motion; evenly spread anvil cloud pumping outflow right across aircraft tracks.
<i>Colorado Region</i>								
18 May	20:20	23:44	00:00, 19 May	−100.68, 41.13	1,144 ^e	48	12	Isolated storm with motion in the downwind direction.
12 June ^d	19:05	00:15	00:00, 13 June	−101.70, 35.23	1,971 ^e	89	23	Isolated storm with motion in the downwind direction.
22 June	22:15	02:00	21:53	−102.752, 40.119	2,563	72	24	Isolated storm with motion in the downwind direction; Smoke ingested from the CO High Park fire.

^aStorm start times correspond to when convection and lightning activity started.

^bStorm end times correspond to when the aircraft finished sampling anvil outflow.

^cMaximum updraft velocity is calculated as $\sqrt{2 \cdot \text{CAPE}}$.

^dStorms sampled solely by the Falcon aircraft.

^eIn-field soundings unavailable for these storms; CAPE (convective available potential energy) determined from the closest routine sounding launched from North Platte, NE (LBF site) on 18 May and Amarillo, Texas (AMA site) on 12 June.

molecules (or moles) of NO_x divided by the relevant number of lightning flashes for the volume-based analysis and mol s⁻¹ divided by the average estimated flash rate (e.g., flashes per second) for the flux-based analysis. Although both methods have been used in the literature, this work is the first to apply both methods to a common data set. The assumptions and uncertainties inherent to each method are evaluated and discussed along each step of the analysis. Finally, in section 4, we compare the results from the volume-based and flux-based analyses of several DC3 storms with storm kinematic properties, lightning flash characteristics, and previously reported results for storms sampled over the U.S. Great Plains since 1976.

2. Experimental Description

2.1. Storm Sampling and Selection

Two instrumented aircraft, the National Science Foundation (NSF)/National Center for Atmospheric Research (NCAR) Gulfstream-V (hereafter referred to as “G-V”) and the NASA DC-8, conducted a total of 17 coordinated, daytime research flights during DC3. Among these flights, five were aimed at sampling the fresh anvil outflow from storms that developed over Oklahoma and northern Texas (referred to henceforth as the Oklahoma region), five over northeastern Colorado, southeastern Wyoming, and southwestern Nebraska (referred to as the Colorado region), and two over north central Alabama. Further information is available in the DC3 overview [Barth *et al.*, 2015]. For this analysis, we select four of the five storms sampled over the Oklahoma region by the DC-8 and G-V on 19 May, 25 May, 29 May, and 16 June and two of the five storms sampled over the Colorado region on 18 May and 22 June (Table 1). These particular storms are selected for their isolated nature, near-uniform wind speed and wind direction in the upper troposphere, anvil development in the same direction as storm motion, and quantifiable LNO_x enhancements above background NO_x. No storms were selected from the Alabama region due to light and variable wind conditions during sampling that made it difficult to connect inflow and outflow for a specific convective system and due to divided objectives for these flights, which precluded sufficient collection of inflow and outflow data.

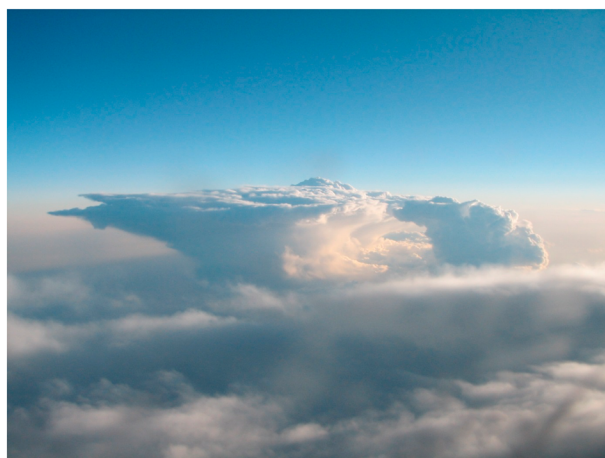


Figure 1. Photograph of a storm over Oklahoma that was not sampled by either aircraft but developed in the same line of convection as the storm sampled on 19 May. Photograph taken on 20 May at 00:15 UTC from the DC-8 aircraft by K. Pickering.

Storms in these regions produce large LNO_x enhancements (~1–2 ppbv) in comparison to low background levels of anthropogenic NO_x (e.g., less than 0.5 ppbv for the Oklahoma region and between 0.5 and 1.5 ppbv for the Colorado region). The planetary boundary layer of these regions also has low to moderate levels of biogenic volatile organic compounds (VOCs) and low to moderately high concentrations of anthropogenic VOCs and carbon monoxide (CO). Selected VOCs and CO can be utilized to quantify vertical transport, as demonstrated in the supporting information (SI).

The third instrumented aircraft, the Deutsches Zentrum für Luft- und Raumfahrt (DLR) Falcon, conducted a total of 13 daytime research flights during DC3, seven of which were aimed at observing fresh anvil outflow from thunderstorms in these geographical regions (H. Huntrieser et al., Injection of lightning-produced NO_x, water vapor, wildfire emissions, and stratospheric air to the UT/LS as observed from DC3 measurements, submitted to *Journal of Geophysical Research: Atmospheres*, 2015a; H. Huntrieser et al., On the origin of pronounced O₃ gradients in the thunderstorm outflow region during DC3, submitted to *Journal of Geophysical Research: Atmospheres*, 2015b). Of the seven flights, only two (e.g., one on 29 May in the Oklahoma region and one on 6 June in the Colorado region) sampled outflow from the same storms as the other two aircraft. However, neither NO nor NO_x measurements were available from the Falcon during these two flights. Although not in concert with the other two aircraft, the Falcon aircraft sampled two storms in the Oklahoma region on 30 May and 5 June and one in the Colorado region on 12 June. While NO and NO_x measurements are available during the 5 June and 12 June storms, only NO measurements are available during the 30 May storm. The storms on 30 May and 12 June developed as strong, isolated convective systems with an elongated anvil in the downwind direction; however, the storm on 5 June was a more complex system with many small individual storm cells embedded in a mesoscale convective vorticity. Owing to the complexity of the 5 June storm, only the 30 May and 12 June storms sampled by the Falcon are included in this analysis (e.g., Table 1). These two cases are described in more detail in H. Huntrieser et al. (submitted to, 2015b).

2.2. Airborne Measurements

Detailed information about the airborne trace gas measurements used in this analysis is summarized in Table 2; NO_x measurements are briefly described here. Airborne measurements of NO were acquired via NO–O₃ chemiluminescence (CL) detection aboard all three aircraft [Ryerson et al., 2000; Ridley and Grahek, 1990; Ziereis et al., 2000]; measurements of NO₂ were mainly acquired using UV photolysis followed by NO–O₃ CL detection [Pollack et al., 2011]. Measurements of NO₂ were also acquired via laser-induced fluorescence aboard the DC-8 [Nault et al., 2015; Thornton et al., 2000] and were used when CL measurements were not available. Airborne measurements are used as reported in the final DC3 data

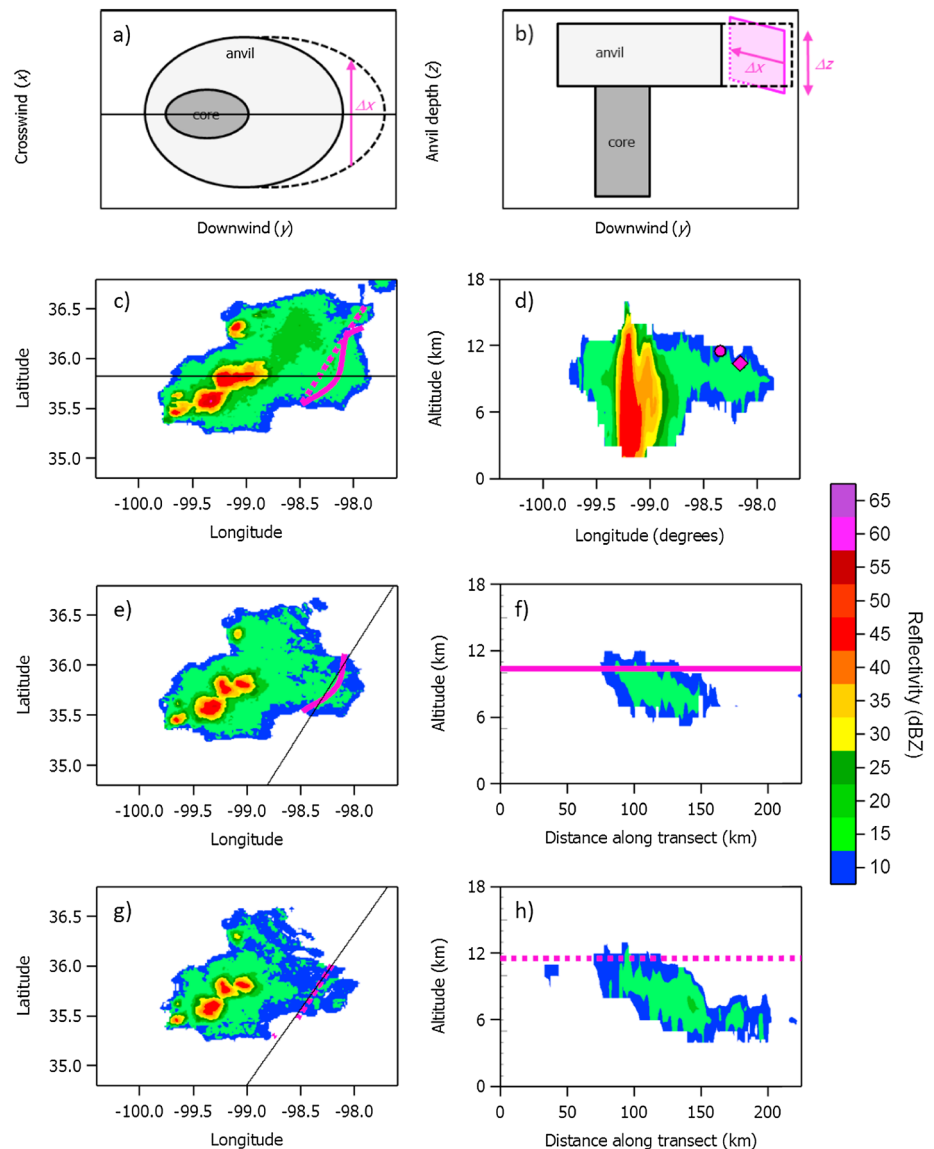


Figure 2. (a and b) Schematic and (c–h) radar representations of the 19 May storm. Top views (left) show the storm core (dark gray and red contours) with respect to an elongated anvil (light gray and green contours) and detrained anvil outflow (area enclosed by dashed lines and light green and blue contours) in the downwind (y) direction. Black lines (left) represent the cut plane for vertical cross sections (right), which illustrate how the depth of the anvil cloud (Δz) is selected for the two-dimensional plane (pink rectangle) used in flux-based calculations. Symbols and lines indicate the location of the two outflow transects performed during this storm (pink diamond and solid pink line for the transect at 10.4 km and pink circle and dotted pink line for the transect at 11.6 km). (Figures 2c and 2d) Composite top view and vertical cross section from 0100 UTC on 20 May; (Figures 2e and 2f) top view of 10 km altitude slice and vertical cross section from 0050 UTC on 20 May; and (Figures 2g and 2h) top view of 11 km altitude slice and vertical cross section from 0110 UTC on 20 May.

archive (<http://www-air.larc.nasa.gov/cgi-bin/ArcView/dc3-seac4rs>); the combination of NO_x , CO, and O_3 measured independently aboard each aircraft is evaluated and compared in the supporting information.

In situ measurements were often acquired simultaneously by the G-V and DC-8 aircraft, with one aircraft performing transects of the outflow between 9 and 13 km above mean sea level (msl), while the other sampled storm inflow between 0.5 and 2 km msl. The lower altitude observing aircraft would often perform a spiraling ascent just outside the storm cloud and complete two to four more crosswind transects of the anvil outflow before returning to Salina, Kansas, the project base for aircraft operations. Combined outflow samplings from multiple aircraft consisted of anywhere between 2 and 12 crosswind transects per storm.

Table 2. Summary of Airborne Trace Gas Measurements Used in This Analysis

Species	Technique	Uncertainty	Frequency	Reference
<i>NASA DC-8</i>				
NO	NO/O ₃ chemiluminescence (CL)	±4%	1 Hz	<i>Ryerson et al. [2000]</i>
NO ₂	UV photolysis followed by NO/O ₃ CL	±6%	1 Hz	<i>Pollack et al. [2011]</i>
NO ₂	Tunable diode laser-induced fluorescence	±10%	1 Hz	<i>Thornton et al. [2000] and Nault et al. [2015]</i>
NO _y	Au catalyzed thermal conversion followed by CL	±12%	1 Hz	<i>Ryerson et al. [1999]</i>
O ₃	NO/O ₃ CL	±3%	1 Hz	<i>Ryerson et al. [1998]</i>
CO	Diode laser spectrometer	±2%	1 Hz	<i>Sachse et al. [1991]</i>
CH ₄	Diode laser spectrometer	±5%	1 Hz	<i>Sachse et al. [1991]</i>
Acetone, propanal	PTR-MS	±10%	^a	<i>de Gouw and Warneke [2007]</i>
<i>NSF/NCAR G-V</i>				
NO	NO/O ₃ CL	±10%	1 Hz	<i>Ridley and Grahek [1990]</i>
NO ₂	UV photolysis followed by NO/O ₃ CL	±15%	1 Hz	<i>Ridley and Grahek [1990]</i>
O ₃	NO/O ₃ CL	±5%	1 Hz	<i>Ridley et al. [1992]</i>
CO	Vacuum UV fluorescence	±3%	1 Hz	<i>Gerbig et al. [1999]</i>
CH ₄	Wavelength-scanned cavity ring-down spectrometer	±5%	1 Hz	<i>Chen et al. [2010]</i>
Acetone, propanal	Gas chromatograph mass spectrometer	±20%	^a	<i>Apel et al. [2015]</i>
<i>DLR Falcon</i>				
NO	NO/O ₃ CL	±30%	1 Hz	<i>Ziereis et al. [2000] and Baehr et al. [2003]</i>
NO _x	UV photolysis followed by NO/O ₃ CL	±30%	1 Hz	<i>Pollack et al. [2011]</i>
O ₃	UV absorption	±5%	1 Hz	<i>Baehr et al. [2003]</i>
CO	Vacuum UV fluorescence	±5%	1 Hz	<i>Gerbig et al. [1999]</i>

^aSpeciated VOCs are measured for 1 s every 20 s by the PTR-MS aboard the DC-8 aircraft; VOCs are measured for 35 s every 2 min using the GC-MS aboard the G-V aircraft.

Owing to its shorter flight duration, the Falcon did not measure storm inflow and often performed fewer than four transects of anvil outflow before returning to base. Although, the Falcon generally performed transects closer to the convective core in comparison to the other two aircraft. For this analysis, we define a crosswind transect of the outflow as a unidirectional pass at a single altitude through the anvil cloud with wind direction nearly normal to the true heading of the aircraft, as illustrated in Figure 2. Hence, the time segments of data points making up each outflow transect are initially parsed according to aircraft altitude, position, and heading. Data points retained from inflow passes are selected according to the spatial and temporal location of the aircraft and the wind direction measured from the aircraft with respect to the radar and visible satellite images of the developing storm.

As described previously by *Ridley et al. [1996]*, substantial enhancement in lightning-produced NO relative to background air occurs only within the anvil cloud. *Huntrieser et al.* (Injection of lightning-produced NO_x, water vapor, wildfire emissions, and stratospheric air to the UT/LS as observed from DC3 measurements, submitted to *Journal of Geophysical Research: Atmospheres*, 2015; On the origin of pronounced O₃ gradients in the thunderstorm outflow region during DC3, submitted to *Journal of Geophysical Research: Atmospheres*, 2015) and section 3.2 of this work further show little evidence of LNO_x enhancement in clear air just below and outside the anvil. Based on these observations, two upfront assumptions are applied to this analysis: (1) all of the NO_x produced by lightning flashes associated with a given storm are contained within the anvil cloud and (2) there is minimal transport of NO_x out of the cloud on the timescale between the onset of lightning activity and when the aircraft sampled the outflow. Therefore, the data points retained from each outflow for analysis are further refined according to when each aircraft is sampling in cloud. Following the work of *Ridley et al. [1996]*, we use increases in particle concentration and/or ice water content measured by cloud probes aboard each aircraft as an in situ indicator for in-cloud sampling. Details of a cloud indicator synthesized for this analysis and a brief description of the cloud probe data products from each aircraft are given in the supporting information.

Lastly, to reduce dilution of measured NO_x by air masses entrained from outside the envelope of the storm (e.g., mixing with stratospheric air from outside the anvil cloud along the cloud edges), data points retained for analysis are further limited to those corresponding with O₃ < 100 ppbv. For these reasons, we do not consider a fifth storm sampled over the Oklahoma region during DC3 on 1 June nor the three storms in the Colorado region on 5 June, 6 June, and 15 June in this analysis owing to all of the outflow transects being performed in part clear air and part cloud along the edge of the anvil cloud.

2.3. Ground and Satellite-Based Measurements

2.3.1. Radar and Satellite Imagery

Radar observations, obtained from stations operated by the National Weather Service within the Next Generation Weather Radar (NEXRAD) program Weather Surveillance Radar, 1988 Doppler network in the continental United States [Crum and Alberty, 1993], are used to determine the three-dimensional spatial extent of each storm. For each flight domain, reflectivity data from individual radars are merged into three-dimensional composites with 2 km horizontal and 1 km vertical resolution every 5 min following the methods of Homeyer [2014] and Homeyer and Kumjian [2015]. Composite images (e.g., Figure 2) show radar reflectivity (colored contours) with 5 dBZ resolution and a minimum detectable reflectivity of 10 dBZ corresponding to precipitating droplets and ice particles. We also use visible and infrared satellite images from the National Oceanic and Atmospheric Administration (NOAA) Geostationary Operational Environmental Satellite (GOES) system [Menzel and Purdom, 1994] to monitor storm development and progression and aid in distinguishing visible cloud from the precipitating cloud detected by the radar. Satellite images are available roughly every 15 min from the online DC3 data archive (http://catalog.eol.ucar.edu/cgi-bin/dc3_2012/ops/index).

2.3.2. Lightning Detection

Three-dimensional mapping of lightning channel segments over Oklahoma and Colorado is available from Lightning Mapping Arrays (LMAs) [Rison *et al.*, 1999]. Lightning measurements for the Oklahoma region were provided by the Oklahoma Lightning Mapping Array (OKLMA), which consisted of a cluster of 12 stations for detecting VHF sources in central Oklahoma and a cluster of 7 stations in southwestern Oklahoma (<http://www.nssl.noaa.gov/tools/oklma/>). Measurements for Texas were provided by the West Texas Lightning Mapping Array (WTLMA) centered in Lubbock, Texas, which consisted of a cluster of 12 VHF source detection stations. Lightning measurements for the Colorado region were provided by the Colorado Lightning Mapping Array (COLMA), which consisted of a single cluster of 16 stations for detecting VHF sources. For the central Oklahoma cluster of stations, Lund *et al.* [2009] indicated that flashes were detected with high efficiency to 200 km from the center of the network. The additional OKLMA stations and the WTLMA perform similarly, while the COLMA is a larger and somewhat more sensitive network. Therefore, this study uses LMA data within 200 km. Further processing sorted the LMA data into flashes, as described by Bruning and MacGorman [2013] and Bruning and Thomas [2015]. This study uses counts of the total number of lightning flashes (IC + CG flashes), as well as the areas of those flashes. We only consider flashes with at least 10 VHF sources to minimize counting flashes resulting from spuriously located sources or from only one or a few located sources. For each flash, the latitude, longitude, and altitude of the flash's initiation are taken as the first VHF source in the flash [Bruning and MacGorman, 2013]. For storms sampled outside the detection radius of the LMA, total flashes (e.g., CG + IC flashes) are estimated from the number of CG flashes detected by the National Lightning Detection Network (NLDN), as further described in section 3.3.

3. Analysis and Results

3.1. Quantifying LNO_x Enhancements

A time series of chemical tracers and cloud indicators for selected storms in the Oklahoma region, depicted in Figure 3, shows enhancements in NO_x associated with lightning-produced NO measured in the outflow of each storm during aircraft penetrations of the anvil cloud. Time series for the remaining Oklahoma and Colorado storms are shown in Figures S6 and S7 of the supporting information. The start/stop time and average altitude, wind speed, ambient pressure, and ambient air temperature measured by the aircraft during each transect are reported in Table 3. During one exemplary storm on 19 May depicted in Figure 3a, the DC-8 aircraft started out by sampling storm inflow, while the G-V aircraft sampled storm outflow. After the G-V aircraft departed the storm region, the DC-8 performed a spiraling ascent to 10.4 km and made two additional outflow transects before returning to base. The gray shaded regions of the figure indicate when the aircraft were sampling in cloud and suggest that the DC-8 aircraft was more often in cloud than the G-V while sampling the 19 May storm. Little variation in O₃ (average of 77 ppbv) and CO (average of 121 ppbv) measured during both DC-8 outflow passes signifies that a well-mixed air mass with little influence from stratospheric air was sampled during the in-cloud portions of the DC-8 transects. Sharp changes in O₃ and CO mixing ratio

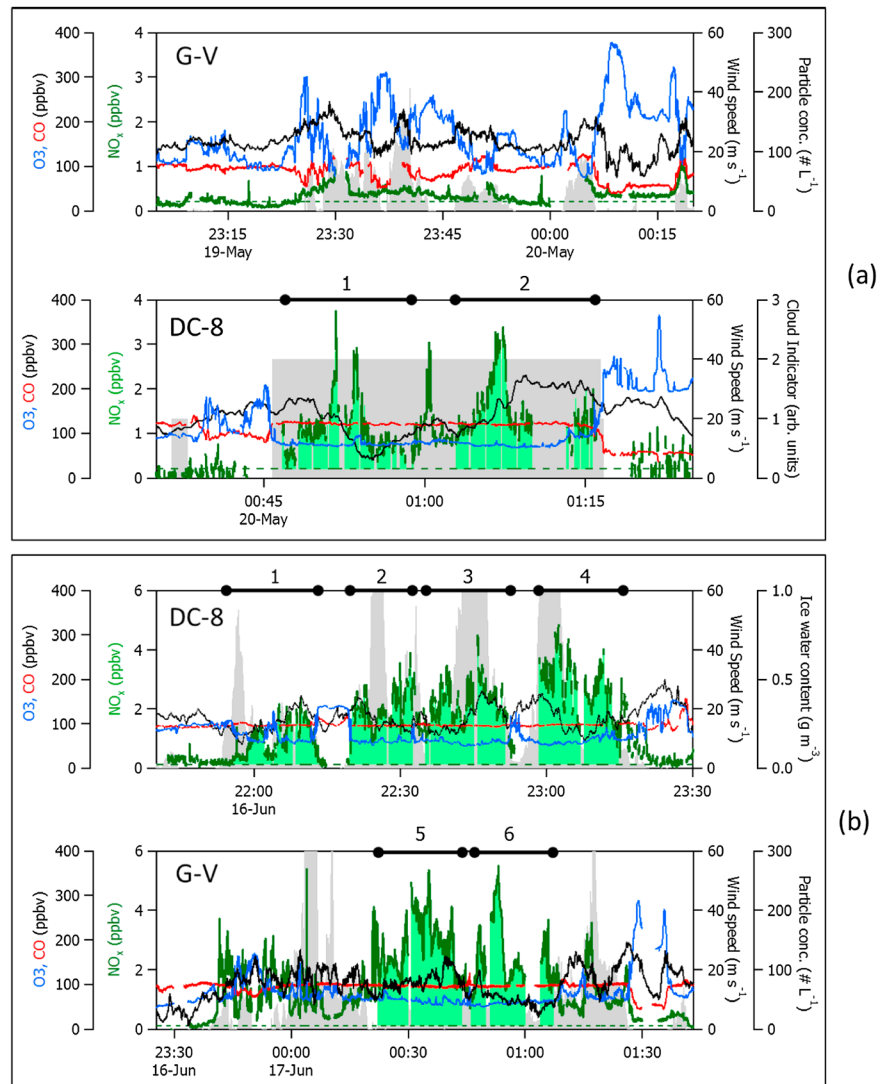


Figure 3. Time series of NO_x (green), O_3 (blue), CO (red), wind speed (black), and a cloud indicator (gray shaded area) measured by the G-V and DC-8 aircraft while sampling the outflow of (a) the 19 May storm and (b) the 16 June storm. Outflow transects for each storm (thick black lines) are numbered sequentially in time. LNO $_x$ enhancements for data points retained from each transect (light green sticks) represent NO_x measured in the outflow (solid green line) minus anthropogenic NO_x transported upward (dashed green line).

correlated with increases/decreases in cloud indicator highlight the transitions between clear air and cloud along each transect. Transects performed by the G-V aircraft during the 19 May storm were largely along the edge of the anvil cloud. High mixing ratios of O_3 observed during these transects indicate wrapping of stratospheric air outside and beneath the anvil, a phenomenon observed for several storms during DC3 and reported by Pan *et al.* [2014] and H. Huntrieser *et al.* (submitted to, 2015a, 2015b). In contrast, the remaining storms sampled in the campaign included more outflow transects and deeper penetrations into the thick part of the anvil cloud (e.g., the 16 June storm in Figure 3b). With the exception of the 30 May and the 22 June storms, nearly constant mixing ratios of O_3 and CO are observed during all in-cloud transects. Variable CO mixing ratios ranging from 100 to 300 ppbv observed during outflow transects of the 22 June storm, depicted in Figure S7 of the SI, reflect convective transport of smoke from the nearby High Park fire in Northern Colorado [Apel *et al.*, 2015].

In order to accurately quantify LNO $_x$ enhancements above background, we use NO_x to CO correlation analysis to calculate the amount of boundary layer NO_x transported upward by each storm. Scatterplots of NO_x

Table 3. Input Parameters and Results of the Volume-Based Approach

Start-End Time (UTC)	Aircraft	Alt (km)	WNS ($m s^{-1}$)	P (hPa)	T (K)	LNO_x^{enh} (ppbv)	$n(NO_x)^{enh}$ ($\times 10^{15}$ molecules m^{-3})	V, Radar Only ($\times 10^{13} m^3$)	V, Radar + Sat ($\times 10^{13} m^3$)	% Diff Volume	$N_{tot}(NO_x)$ ($\times 10^{30}$ molecules)	Flash Count (# of flashes)	$R_{Vol}(NO_x)$ ($\times 10^{-5}$ molecules $flash^{-1}h$)
Oklahoma Region													
<i>19 May Storm, Avg. Anthro. $NO_x = 0.22 \pm 0.07$ ppbv</i>													
00:46:09–00:59:01	DC-8	10.4	17.0	262.2	226.6	0.84 ± 0.32	7.3 ± 2.8	14.5 ± 2.2	16.6 ± 3.3	13	1.2 ± 0.5	5,056 ± 400	24.0 ± 10.3
01:02:57–01:15:50	DC-8	11.6	26.3	219.1	219.9	1.36 ± 0.48	10.1 ± 3.6	14.4 ± 2.2	16.2 ± 3.3	11	1.6 ± 0.7	5,746 ± 500	28.5 ± 11.5
Weighted mean													
00:42:26–00:49:44	G-V	12.1	31.8	206.8	220.2	0.38 ± 0.23	2.7 ± 1.6	14.5 ± 2.0	16.0 ± 2.7	9	0.4 ± 0.3	9,949 ± 586	4.3 ± 2.7
01:19:10–01:32:20	DC-8	11.2	25.9	235.5	224.8	0.97 ± 0.39	7.6 ± 3.1	18.3 ± 2.8	20.2 ± 3.6	9	1.5 ± 0.7	12,758 ± 209	12.0 ± 5.3
01:31:26–01:35:39	G-V	11.8	27.6	217.0	222.0	0.84 ± 0.33	6.2 ± 2.4	18.8 ± 2.9	21.7 ± 3.5	13	1.3 ± 0.6	12,959 ± 155	10.4 ± 4.3
Weighted mean													
<i>25 May Storm, Avg. Anthro. $NO_x = 0.30 \pm 0.10$ ppbv</i>													
23:13:52–23:20:07	G-V	11.1	33.7	238.7	227.0	0.57 ± 0.38	4.5 ± 3.0	12.7 ± 1.6	14.0 ± 2.3	9	0.6 ± 0.4	9,236 ± 1,100	6.8 ± 4.8
23:32:20–23:44:58	G-V	11.4	35.6	227.6	225.4	0.53 ± 0.38	4.0 ± 2.9	17.6 ± 2.2	19.5 ± 3.2	10	0.8 ± 0.6	14,602 ± 1,277	5.3 ± 4.1
23:42:43–23:54:50	DC-8	10.9	33.0	245.3	228.4	1.21 ± 0.54	9.7 ± 4.3	18.8 ± 2.3	20.4 ± 3.3	8	2.0 ± 0.9	16,995 ± 1,257	11.6 ± 5.5
23:51:59–00:05:11	G-V	11.7	32.6	217.7	224.2	0.49 ± 0.37	3.6 ± 2.7	22.4 ± 2.6	23.6 ± 3.5	5	0.8 ± 0.7	19,911 ± 1,582	4.3 ± 3.3
00:16:50–00:23:34	G-V	11.7	37.1	216.7	224.0	0.79 ± 0.43	5.7 ± 3.2	26.7 ± 3.0	27.8 ± 3.7	4	1.6 ± 0.9	24,733 ± 1,656	6.4 ± 3.7
00:22:20–00:35:38	DC-8	10.8	31.8	250.1	229.3	0.74 ± 0.42	6.0 ± 3.4	28.6 ± 3.2	30.9 ± 4.3	6	1.9 ± 1.1	29,791 ± 1,743	6.2 ± 3.7
00:34:13–00:41:21	G-V	12.1	35.2	204.8	222.3	0.98 ± 0.48	6.7 ± 3.3	30.9 ± 3.4	32.9 ± 4.4	6	2.2 ± 1.1	31,551 ± 1,752	7.0 ± 3.6
Weighted mean													
<i>30 May Storm^{cf}, Avg. Anthro. $NO_x = 0.33 \pm 0.28$ ppbv</i>													
00:11:02–00:21:27	Falcon	10.0	25.6	282.3	234.2	1.16 ± 0.70	10.4 ± 6.4	18.5 ± 2.5	21.1 ± 3.3	12	2.2 ± 1.4	6,826 ± 425 ^f	32.1 ± 20.5
<i>16 June Storm^e, Avg. Anthro. $NO_x = 0.11 \pm 0.09$ ppbv</i>													
21:53:15–22:13:13	DC-8	11.8	15.4	219.9	223.7	0.84 ± 0.30	6.2 ± 2.2	31.1 ± 3.6	164.4 ± 13.5	81	2.3 ± 0.9	22,122 ± 774	10.5 ± 3.9
22:19:39–22:32:29	DC-8	12.0	16.7	213.0	222.4	1.89 ± 0.61	13.6 ± 4.4	34.4 ± 4.0	114.1 ± 13.3	70	5.9 ± 1.9	21,359 ± 408	26.3 ± 9.1
22:35:14–22:51:29	DC-8	12.2	17.1	207.0	220.4	2.15 ± 0.68	15.1 ± 4.8	36.8 ± 4.4	115.0 ± 13.0	68	6.7 ± 2.3	27,520 ± 712	24.2 ± 8.3
22:58:31–23:14:46	DC-8	12.2	17.0	207.0	220.6	2.67 ± 0.84	18.8 ± 5.9	40.7 ± 5.1	105.3 ± 12.5	61	9.2 ± 3.1	31,217 ± 759	29.4 ± 10.0
23:52:51–00:06:31	G-V	12.2	16.6	207.8	220.2	2.75 ± 0.86	19.4 ± 6.1	39.6 ± 5.2	90.3 ± 11.0	56	9.2 ± 3.1	38,558 ± 859	28.9 ± 8.2
00:07:47–00:20:38	G-V	11.6	10.0	227.6	224.6	2.37 ± 0.75	18.0 ± 5.7	37.6 ± 5.0	105.4 ± 10.7	64	8.1 ± 2.8	41,314 ± 741	19.7 ± 6.8
Weighted mean													
<i>18 May Storm, Avg. Anthro. $NO_x = 0.20 \pm 0.06$ ppbv^b</i>													
23:16:58–23:22:28	DC-8	11.2	22.6	228.3	218.0	0.81 ± 0.34	6.4 ± 2.6	8.2 ± 1.3	12.8 ± 2.4	36	0.8 ± 0.4	7,188 ± 193	11.4 ± 5.0
23:22:31–23:31:12	DC-8	11.2	20.8	227.6	217.7	0.68 ± 0.30	5.3 ± 2.4	8.3 ± 1.3	12.2 ± 2.5	32	0.6 ± 0.3	7,580 ± 177	8.5 ± 4.2

Table 3. (continued)

Start-End Time (UTC)	Aircraft	Alt (km)	WNS (ms^{-1})	P (hPa)	T (K)	$\text{LNO}_x^{\text{enh}}$ (ppbv)	$n(\text{NO}_x^{\text{enh}})$ ($\times 10^{15}$ molecules m^{-3})	V_r Radar Only ($\times 10^{13}$ m^3)	V_r Radar + Sat ($\times 10^{13}$ m^3)	% Diff Volume	$N_{\text{vol}}(\text{NO}_x)$ ($\times 10^{30}$ molecules)	Flash Count (# of flashes)	$P_{\text{vol}}(\text{NO}_x)$ ($\times 10^{-5}$ molecules flash^{-1}) ^h
23:31:20–23:36:11	DC-8	11.2	26.6	227.3	217.5	0.48 ± 0.25	3.8 ± 2.0	8.3 ± 1.3	12.2 ± 2.5	32	0.5 ± 0.3	7,750 ± 157	6.0 ± 3.4
23:36:30–23:44:17	DC-8	11.2	22.9	227.6	217.5	0.47 ± 0.25	3.7 ± 1.9	8.3 ± 1.3	12.4 ± 2.7	33	0.5 ± 0.3	8,003 ± 99	5.7 ± 3.2
Weighted mean													6.1 ± 1.6
<i>12 June Storm^{f,g}, Avg. Anthro. $\text{NO}_x = 0.21 \pm 0.12$ ppbv^a</i>													
23:23:21–23:32:11	Falcon	10.1	27.4	274.9	230.0	0.99 ± 0.67	8.9 ± 6.0	--	--	--	--	9,055 ± 33	--
23:34:15–23:46:19	Falcon	11.3	30.0	232.2	221.1	1.07 ± 0.71	8.4 ± 5.6	--	--	--	--	10,550 ± 27	--
23:50:50–00:03:07	Falcon	11.9	38.4	209.9	217.0	1.88 ± 1.15	13.6 ± 8.4	--	--	--	--	13,230 ± 93	--
00:05:16–00:13:38	Falcon	12.3	40.0	199.2	215.0	1.70 ± 1.06	11.8 ± 7.3	--	--	--	--	14,494 ± 231	--
Weighted mean													
<i>22 June Storm^d, Avg. Anthro. $\text{NO}_x = 0.17 \pm 0.07$ ppbv</i>													
23:31:09–23:43:10	G-V	11.8	32.2	217.0	223.2	0.58 ± 0.23	4.2 ± 1.7	--	--	--	--	9,432 ± 803	--
23:46:08–23:56:05	G-V	11.2	33.7	239.0	227.0	0.31 ± 0.16	2.4 ± 1.3	--	--	--	--	10,858 ± 517	--
23:59:05–00:10:12	G-V	10.6	30.1	262.4	231.0	0.10 ± 0.11	0.8 ± 0.9	--	--	--	--	12,102 ± 425	--
00:12:26–00:25:43	G-V	11.5	33.4	227.9	224.7	0.62 ± 0.25	4.7 ± 1.9	--	--	--	--	13,604 ± 531	--
00:20:34–00:35:29	DC-8	11.2	28.3	238.5	225.9	0.80 ± 0.35	6.3 ± 2.8	11.1 ± 1.6	13.6 ± 2.2	18	0.9 ± 0.4	14,678 ± 592	5.8 ± 2.8
00:27:53–00:37:28	G-V	11.8	28.0	217.0	222.0	0.82 ± 0.31	6.0 ± 2.3	11.1 ± 1.6	13.6 ± 2.2	18	0.8 ± 0.3	15,293 ± 538	5.3 ± 2.2
00:35:29–00:46:04	DC-8	10.8	28.1	250.4	228.1	0.82 ± 0.36	6.8 ± 3.0	11.5 ± 1.7	17.0 ± 3.7	32	1.2 ± 0.6	15,739 ± 430	7.3 ± 3.6
00:51:11–01:00:38	DC-8	10.5	34.3	261.8	230.7	0.95 ± 0.40	8.1 ± 3.4	12.3 ± 1.9	19.6 ± 3.7	37	1.6 ± 0.7	16,820 ± 202	9.4 ± 4.3
00:58:08–01:12:09	G-V	11.2	28.7	238.7	226.5	0.60 ± 0.24	4.7 ± 1.9	12.9 ± 2.0	21.8 ± 3.7	41	1.0 ± 0.4	17,155 ± 237	6.0 ± 2.6
01:03:27–01:12:19	DC-8	10.9	32.8	249.7	228.0	1.63 ± 0.60	13.4 ± 4.9	12.9 ± 2.0	21.8 ± 3.7	41	2.9 ± 1.2	17,155 ± 237	17.0 ± 6.7
01:15:58–01:28:57	DC-8	10.9	32.8	249.1	228.0	1.14 ± 0.45	9.4 ± 3.7	13.6 ± 2.1	22.0 ± 4.1	38	2.1 ± 0.9	19,191 ± 627	10.8 ± 4.6
01:51:34–02:03:08	G-V	11.2	35.6	238.8	227.0	0.83 ± 0.31	6.5 ± 2.4	--	--	--	--	23,379 ± 354	--
Weighted mean													8.6 ± 1.5

^aAverage NO_x transported upward is determined from NO_x measurements upwind and just outside of the storm cloud.

^bAverage NO_x transported upward is based on inflow observations during the 12 June and 22 June storms that also occurred in the Colorado region.

^c $\text{LNO}_x^{\text{enh}}$ for this storm are determined from measurements of NO only.

^dStorm-transported smoke from the Colorado High Park fire.

^eSatellite-corrected volumes are grossly overestimated for the 16 June storm; therefore, radar-based volumes adjusted by the average 20% underestimate for using radar alone are used for subsequent $N_{\text{vol}}(\text{NO}_x)$ and $P_{\text{vol}}(\text{NO}_x)$ calculations.

^fDue to poor spatial coverage by the LMA, lightning flash counts for these storms are calculated from CG flashes detected by the NLDN.

^gVolume estimates for the 12 June storm are not available due to storm development in a NEXRAD domain with limited coverage.

^hUncertainties in $P_{\text{vol}}(\text{NO}_x)$ determined for each transect represent the quadrature combination of uncertainties in $n(\text{NO}_x^{\text{enh}})$, V_r , and flash count. A weighted average reported for each storm reflects the average results from the individual transects of that storm weighted by the inverse square of their fractional uncertainties.

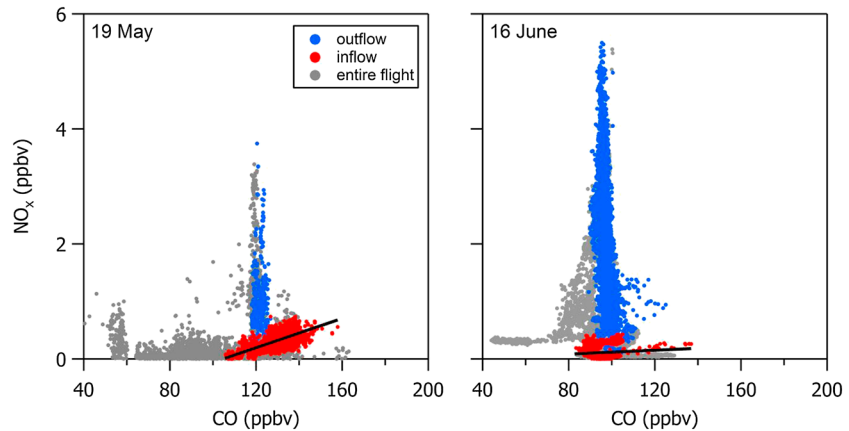


Figure 4. Exemplary scatterplots of NO_x versus CO measured by the DC-8 aircraft during (left) the 19 May storm and by the G-V aircraft during (right) the 16 June storm. Data points represent measurements from the entire flight (gray), inflow transects (red), and outflow transects (blue); solid black lines represent LLS ODR of the inflow data points.

and CO measured during inflow passes (e.g., Figure 4) are fit using linear least squares (LLS) [Press *et al.*, 1988] orthogonal distance regression (ODR) [Boggs *et al.*, 1987]. The average anthropogenic NO_x transported upward from the planetary boundary layer in each storm is calculated from the slope and intercepts from a LLS fit of the inflow data points and the average CO concentration observed in the outflow, as shown in equation (1).

$$\text{NO}_x^{\text{transported}} = \left[\left(\frac{\text{NO}_x}{\text{CO}} \right)_{\text{slope}} \times \text{CO}^{\text{outflow}} \right] + \text{NO}_x^{\text{intercept}} \quad (1)$$

This calculation assumes a constant CO background and that variability in CO mixing ratio arises solely from anthropogenic sources in the planetary boundary layer.

Storm inflow was often sampled by only one aircraft; thus, a single value for NO_x transported upward in each storm (reported in Table 3) is used for further calculations. Lacking low-altitude inflow measurements from the Falcon aircraft, we use the average NO_x determined from a few data points collected upwind and outside of cloud as the aircraft approached each storm to estimate the average background NO_x . We assume 0.1 ppbv of NO and 0.2 ppbv of NO_x that originated from the boundary layer during the 30 May storm sampled over the Oklahoma region and the 12 June storm sampled over the Colorado region, respectively. A similar assumption (i.e., NO_x transported upward = 0.2 ppbv) is applied to the Colorado storm sampled on 18 May, where NO_2 measurements from the DC-8 were unavailable, while the aircraft was sampling storm inflow. Uncertainties for NO_x transported upward in storms sampled by the DC-8 and G-V are calculated by propagating the 1σ standard deviations in the slope, y-intercept, and average CO mixing ratio from the LLS fit in quadrature with the overall NO_x and CO measurement uncertainties (e.g., 30% for NO_x and 5% for CO) determined from intercomparison of the airborne sensors (e.g., Text S2 in the supporting information). Uncertainties for NO_x transported upward in storms sampled by the Falcon reflect the quadrature combination of the 1σ standard deviation in the average NO_x measured upwind and outside of cloud (e.g., 10% for 30 May) and a measurement uncertainty of 55% determined from intercomparison with the DC-8.

Average LNO_x enhancements, $\text{LNO}_x^{\text{enh}}$, reported in Table 3, are then determined by subtracting NO_x transported upward in each storm from the average NO_x measured in each outflow transect. For further analysis in the following sections, $\text{LNO}_x^{\text{enh}}$ is converted to units of molecules m^{-3} , denoted as $n(\text{NO}_x)^{\text{enh}}$ in Table 3, using the average pressure and temperature reported for each transect and then to moles m^{-3} using Avogadro's number. Error bars for $\text{LNO}_x^{\text{enh}}$ reflect propagated uncertainties from the average NO_x transported upward by each storm, as described above, and the average NO_x measured in the outflow. The latter accounts for uncertainties in the NO_x measurements from the aircraft but does not account for variability about the mean from each transect. Therefore, we also report a weighted mean $\text{LNO}_x^{\text{enh}}$, denoted as \bar{X} in

equation (2), and corresponding variability about the mean, denoted as $\sigma(\bar{X})$ in equation (3), for each storm. The individual $\text{LNO}_x^{\text{enh}}$ from each transect, denoted as x_i in equation (2), are weighted by the inverse square of their fractional uncertainties, denoted by w_i in equations (2) and (3) [Taylor, 1997].

$$\bar{X} = \frac{\sum_{i=1}^n w_i x_i}{\sum_{i=1}^n w_i} \quad (2)$$

$$\sigma(\bar{X}) = \sqrt{\frac{1}{\sum_{i=1}^n w_i}} \quad (3)$$

The physical characteristics of the storm play an important role in being able to quantify $\text{LNO}_x^{\text{enh}}$. An ideal storm would have sufficient updraft velocity to pump LNO_x upward and sufficient wind speed aloft to elongate the anvil cloud across the aircraft sampling path allowing LNO_x to be sampled at a safe downwind distance from the core. A physical picture of a near-ideal system with a well-defined core, cloud base, and elongated anvil cloud in the downwind direction is shown in the exemplary photograph in Figure 1 and indicated by the radar images for the 19 May storm in Figure 2. Images from other storms selected for this analysis (not shown) demonstrate similar physical characteristics. All of the storms in the Oklahoma and Colorado regions had sufficient updraft velocities (e.g., potential maximum updraft velocities calculated as $\sqrt{2 \cdot \text{CAPE}}$ and ranging from 50 to 85 m s^{-1} as described in the supporting information) to rapidly transport LNO_x over a 10 km vertical range in a few minutes or less (Table 1). Rapid upward transport in these storms is consistent with previous studies of a Colorado storm sampled during the Stratospheric-Tropospheric Experiment: Radiation, Aerosols, and Ozone (STERAO) study in 1996 [Skamarock et al., 2000], where model simulations showed that the majority of air parcels ascended to anvil heights in roughly 10 min. In addition, storms with larger wind speeds aloft should be sufficient to elongate the anvil cloud such that NO_x in storm outflow can be well sampled by the aircraft. Vertical wind shear for DC3 storms ranges from 12 to 27 m s^{-1} (Table 1), and the corresponding average wind speeds measured during anvil outflow transects range from 10 to 40 m s^{-1} (Table 3). The effect of wind speeds aloft on this analysis is discussed further in section 4.1.

On the other hand, the method by which each storm is sampled plays a considerable factor in this analysis. The ideal data set would include upwind, inflow samplings at a range of altitudes just outside the storm cloud as well as multiple crosswind and downwind transects in the anvil cloud at various altitude levels. While avoiding an unsafe turbulent core, the objective would be to three-dimensionally map entrainment, transport, anvil outflow, downwind transport, and the horizontal and vertical distributions within each storm. Although crosswind transects of storm outflow in cloud are limited for DC3 storms (e.g., due to the difficulty in predicting the movement of the storms, other scientific objectives that required sampling downwind of the storm or in clear air, the allotted flight duration, and air traffic control), the use of two instrumented aircraft allowed at least 2 to 12 crosswind transects to be acquired per storm (e.g., Table 3).

While NO_x transported upward from the mixed boundary layer is represented using the inflow transects performed by a single aircraft below 4 km msl., a lack of cloud-penetrating transects performed between 4 and 8 km leaves little information about lateral entrainment, downward transport, and the detailed horizontal and vertical NO_x distributions. Following Chameides et al. [1987], we assume minimal advection of $\text{LNO}_x^{\text{enh}}$ out of the anvil via storm downdrafts. Based on previous analyses of a Colorado storm during STERAO [Skamarock et al., 2003] that indicated that most of the NO_x produced by lightning is transported upward and into the expanding anvil cloud, we assume that lateral entrainment in addition to downward transport does not significantly affect NO_x mixing ratios measured in the anvil outflow. This is a reasonable assumption based on the vertical distribution of sources of LNO_x . IC lightning flashes predominantly occur in the anvil region, while CG flashes peak at about -15°C [DeCaria et al., 2005]. For the 29 May storm, we find that the peak of the vertical distribution for both IC and CG flashes spans roughly 7 to 13.5 km giving a vertical depth of ~ 6.5 km. Combining entrainment rates of $< 10\% \text{ km}^{-1}$ (A. Fried et al., Convective transport of formaldehyde to the upper troposphere and lower stratosphere and associated scavenging in thunderstorms over the central United States during the 2012 DC3 study, submitted to *Journal of Geophysical Research: Atmosphere*, 2015) over this vertical depth with an average IC:CG ratio of 4.5 for the Oklahoma and Colorado regions [Bocippio et al., 2001], NO_x entrained from the environment is expected to have only a small impact ($< 10\%$) on NO_x mixing ratios measured in the anvil.

We also consider the effects of NO_x gain and loss chemistry on outflow NO_x measured in DC3 storms. The concentration of NO_x in the atmosphere depends on the source strength, the rates of NO_x oxidation reactions, and the rates of removal of the oxidation products [Seinfeld and Pandis, 2006]. While NO_x , peroxyacetyl nitrate (PAN), and O_3 will be nearly conserved during in-cloud transport, soluble species like nitric acid (HNO_3) are likely to be removed by wet scavenging, precipitation, or formation of particulate nitrate [Ridley *et al.*, 1996]. In contrast, photolysis of HNO_3 and thermal decomposition of PAN can lead to reproduction of NO_x . Longer lifetimes in the upper troposphere and rapid upward transport, which leave little time for chemical conversion of NO_x prior to aircraft sampling, allow anthropogenic NO_x transported upward and LNO_x enhancements produced by the storm to be well characterized. Therefore, we expect minimal gains and losses in NO_x , and thus little effect from oxidant chemistry, on measured NO_x mixing ratios.

3.2. Converting to Molecules of LNO_x

In the following sections, we apply and evaluate two approaches for converting volume-based mixing ratios of LNO_x enhancements to LNO_x production in molecules (or moles) of NO_x . As shown above, the storms highlighted in this analysis should have sufficient wind speed aloft to elongate the anvil cloud across the sampling path of the aircraft. Therefore, a static method of measuring average mixing ratios and a dynamic method of measuring a flux should sample the same amount of lightning NO_x enhanced air and thus result in similar values for molecules (or moles) of LNO_x.

3.2.1. Volume-Based Method

The first approach for converting an average volume-based mixing ratio associated with measured LNO_x enhancements, $n(\text{NO}_x)^{\text{enh}}$, in units of molecules m^{-3} , to molecules of NO_x produced by lightning in a given storm, $N_{\text{vol}}(\text{NO}_x)$, uses an estimated volume, V , in units of cubic meters, into which the LNO_x has been distributed, as shown in equation (4).

$$N_{\text{vol}}(\text{NO}_x) = n(\text{NO}_x)^{\text{enh}} \times V \quad (4)$$

This volume-based approach follows the procedures described by Ridley *et al.* [1996, 2004] and assumes that LNO_x is equally distributed into a specified volume defined by the spatial extent of the visible cloud. Previous studies [Dye *et al.*, 2000; Ridley *et al.*, 1996; Skamarock *et al.*, 2000] suggest that very little of the LNO_x-enhanced air mass is pumped out of the anvil on the timescale between LNO_x production and measurement of these convectively active systems by the aircraft. As moist air is continuously convected upward, the anvil gets increasingly larger in size, with the boundary of the anvil cloud distinguished by ice or other cloud particles. For cases with little wind shear, the anvil cloud grows upward and symmetrically outward (e.g., a circular-shaped anvil); in cases with stronger winds aloft, the anvil is elongated asymmetrically and increases in size (e.g., Figures 1 and 2). In situ observations from DC3 support these storm dynamics. A downwind transect performed by the G-V aircraft during the 16 June Oklahoma region storm (e.g., Figure 3b between 01:20 and 01:30 UTC on 17 June) demonstrates elevated NO_x concentrations and nearly constant mixing ratios of CO and O_3 when the aircraft is embedded within cloud. A decrease in measured NO_x to background levels and sharp changes in CO and O_3 observed as the aircraft transitions from cloud to clear air at 01:25 UTC demonstrates that the spatial extent of the LNO_x-enhanced air mass is coincident with the spatial extent of the anvil cloud.

The challenge in applying this method, however, lies in accurately determining the three-dimensional extent of a dynamic system. Here we use the available radar and satellite data to estimate the volume of each storm used in this analysis. While the cloud base across the entire extent of each storm can be well characterized solely from the radar observations, the vertical and horizontal extent of the visible cloud are likely to be underestimated from radar alone since radar systems used during DC3 are only capable of detecting precipitating hydrometeors (e.g., radar reflectivity ≥ 10 dBZ), which gradually settle away from their convective source and extend to altitudes lower than the true cloud top [e.g., Homeyer, 2014, Figure 6]. Therefore, we use infrared cloud top temperatures from GOES satellite observations and modeled vertical temperature profiles from the National Centers for Environmental Prediction Global Forecast System to improve representation of the cloud top for volume calculations. These satellite-based estimates for the cloud top are only applied if the cloud top height is greater than that determined from radar alone. Similarly, the horizontal extent of the anvil is corrected using satellite observations only if cloud top altitudes are greater than or equal to the radar-based cloud top near the anvil edge. Based on comparisons between the radar composites and

higher-resolution observations (e.g., CloudSat), the vertical extent of each storm can be estimated to within ± 500 m. Cloud bases are identified as the lowest altitude of radar echo at each grid point and extrapolated horizontally in cases where satellite-only cloud top altitudes of the anvil exist. Since the convective storms temporally evolve, even over a few hours while the aircraft are sampling storm outflow, we calculate a storm volume for each outflow transect at a single time closest to the midtime of that transect and when the radar and satellite data products are temporally coincident. These volumes are reported in Table 3.

Uncertainties in storm volume, related to the ± 500 m altitude uncertainty in cloud base and cloud top, range from 12 to 22% (Table 3) with an average of 15% over all storms. Since $N_{\text{vol}}(\text{NO}_x)$ scales linearly with $n(\text{NO}_x)^{\text{enh}}$ and V , as shown in equation (4), the volume term alone can impart up to 22% uncertainty in $N_{\text{vol}}(\text{NO}_x)$. Combining the uncertainties for $\text{LNO}_x^{\text{enh}}$ and volume from each transect in quadrature results in uncertainties in $N_{\text{vol}}(\text{NO}_x)$ ranging from 33% to 76% and an average of 48% over all storms.

Contrasting satellite-corrected volumes with those estimated from radar alone (Table 3) shows that the volume of the visible cloud for these storms is an average of 20% larger than the volume of the precipitating cloud; thus, using volumes determined from radar alone would lead to underestimates in $N_{\text{vol}}(\text{NO}_x)$ by 20%. Note that in the absence of sufficient radar coverage, there is no volume estimate for the 12 June storm. Satellite-corrected volumes for the 16 June storm (Table 3) are also questionable owing to a large nearby convective system merging with the investigated storm around the time when the aircraft were performing outflow transects making individual cloud top heights difficult to distinguish in the satellite data. Therefore, for the 16 June storm, we use an adjusted radar-based volume (i.e., radar-based volume + 20% of the radar-based volume) to account for the underestimate in V from radar alone for subsequent calculations of $N_{\text{vol}}(\text{NO}_x)$ in Table 3. We also note that there is considerable error in the calculated volume for the 29 May storm after $\sim 23:40$ UTC due to explosive convection that developed northwest of the main line and beneath the downstream anvil. While it is possible that lightning flashes from convection to the northwest could have contributed to the observed LNO_x enhancements for this case, it is only within the scope of this work to calculate the LNO_x enhancements and storm volume associated with the southernmost main line of convection sampled by the aircraft. Consequently, we suspect that the volume, and thus $P_{\text{vol}}(\text{NO}_x)$, could be biased low for the 29 May storm.

3.2.2. Flux-Based Method

The second approach follows the flux-based analyses in *Chameides et al.* [1987] and *Huntrieser et al.* [1998] for converting volume-based mixing ratios of LNO_x enhancements (e.g., moles of NO_x per moles of air) to a flux of LNO_x , F_{LNO_x} , in units of mol s^{-1} . This calculation utilizes $\text{LNO}_x^{\text{enh}}$ and the average rate at which air is advected out of the anvil, as shown in equation (5).

$$F_{\text{LNO}_x} = \text{LNO}_x^{\text{enh}} \times (v_a - v_s) \times \rho_{\text{air}} \times \Delta x \times \Delta z \quad (5)$$

The latter depends on the horizontal wind speed inside the anvil (v_a) in units of m s^{-1} , the velocity of the storm (v_s) in units of m s^{-1} , the air density in the anvil (ρ_{air}) in units of moles of air m^{-3} , and the horizontal width (Δx) and vertical depth (Δz) of the anvil cloud in units of meters. Here we define the horizontal wind speed inside the anvil as the vector component of wind speed normal to the true heading of the aircraft and the velocity of the storm system as the vector component of wind speed at the steering level of the anvil cloud. Since crosswind transects by the aircraft were not always performed normal to the direction of outward growth of the anvil, fluxes are determined here on a 1 s timescale to account for instantaneous changes in wind direction, wind speed, and true heading of the aircraft.

In contrast to the works of *Chameides et al.* [1987] and *Huntrieser et al.* [1998], we find the contribution of v_s in equation (5) to be small for DC3 storms. The aircraft performed transects far enough downwind of the convective core during DC3 that outflow was largely detrained from the convective system prior to being sampled by the aircraft. Therefore, the mass flux of LNO_x through the aircraft's path is likely decoupled from storm movement. Similar wind speeds measured in cloud and in clear air provide evidence that the air has already been detrained from the storm. While this is the case for most DC3 storms (e.g., the time series in Figure 3), it is not the case for all storms used in this analysis (e.g., the storm on 25 May as shown in Figure S6 of the supporting information). While the best approximation of wind speeds for the flux calculations is likely somewhere between v_a and $(v_a - v_s)$, quantifying the contribution of storm motion for each transect is beyond the scope of this work. Results of the flux calculations neglecting storm speed (reported in Table 4) are compared with results of flux calculations including v_s in section S5 of the supporting information.

Table 4. Input Parameters and Results of the Flux-Based Approach

Start/End Time (UTC)	Aircraft	Alt (km)	Anvil Cloud Base (km)	Anvil Cloud Height (km)	F_{LNO_x} (mol s^{-1})	Flash Rate (flashes s^{-1})	$P_{\text{flux}}(\text{NO}_x)^c$ (moles flash $^{-1}$)	$P_{\text{vol}}(\text{NO}_x)^d$ (moles flash $^{-1}$)	% Diff $P(\text{NO}_x)$ (vol.-flux)
<i>Oklahoma Region</i>									
<i>19 May Storm</i>									
00:46:09–00:59:01	DC-8	10.4	7.6	12.0	98 ± 38	0.32	306 ± 132	398 ± 171	23
01:02:57–01:15:50	DC-8	11.6	7.0	13.0	181 ± 65	0.34	532 ± 256	473 ± 192	11
Weighted mean							407 ± 131	437 ± 133	7
<i>25 May Storm</i>									
00:42:26–00:49:44	G-V	12.1	9.2	13.0	86 ± 3.5	1.58	55 ± 22	72 ± 45	24
01:19:10–01:32:20	DC-8	11.2	6.3	13.0	269 ± 93	1.47	183 ± 66	200 ± 88	8
01:31:26–01:35:39	G-V	11.8	8.2	11.9	61 ± 25	1.44	43 ± 17	172 ± 71	75
Weighted mean							84 ± 19	150 ± 41	44
<i>29 May Storm</i>									
23:13:52–23:20:07	G-V	11.1	5.8	15.0	276 ± 91	1.47	188 ± 66	113 ± 80	40
23:32:20–23:44:58	G-V	11.4	5.1	14.0	648 ± 214	1.87	346 ± 135	89 ± 67	74
23:42:43–23:54:50	DC-8	10.9	5.3	14.1	372 ± 125	2.02	184 ± 65	193 ± 92	5
23:51:59–00:05:11	G-V	11.7	6.5	14.0	286 ± 96	2.21	129 ± 45	71 ± 55	45
00:16:50–00:23:34	G-V	11.7	7.0	13.0	330 ± 116	2.50	132 ± 48	106 ± 62	20
00:22:20–00:35:38	DC-8	10.8	6.2	13.8	301 ± 101	2.76	109 ± 37	103 ± 61	5
00:34:13–00:41:21	G-V	12.1	9.3	13.0	118 ± 48	2.84	41 ± 17	116 ± 60	64
Weighted mean							141 ± 19	107 ± 24	−24
<i>30 May Storm^b</i>									
00:11:02–00:21:27	Falcon	10.0	4.7	13.0	66 ± 22	0.69 ^b	96 ± 32	534 ± 341	82
<i>16 June Storm</i>									
21:53:15–22:13:13	DC-8	11.8	8.5	13.0	123 ± 48	2.11	58 ± 23	174 ± 65	66
22:19:39–22:32:29	DC-8	12.0	4.4	13.7	520 ± 171	1.87	277 ± 103	436 ± 150	36
22:35:14–22:51:29	DC-8	12.2	5.3	14.0	593 ± 198	2.18	271 ± 101	402 ± 137	32
22:58:31–23:14:46	DC-8	12.2	2.9	13.5	1019 ± 332	2.21	460 ± 197	488 ± 165	6
23:52:51–00:06:31	G-V	12.2	6.8	11.6	1199 ± 450	2.25	532 ± 263	397 ± 136	25
00:07:47–00:20:38	G-V	11.6	9.6 ^a	11.4 ^a	204 ± 130	2.30	89 ± 57	326 ± 112	73
Weighted mean							205 ± 36	291 ± 41	30
<i>Colorado Region</i>									
<i>18 May Storm</i>									
23:16:58–23:22:28	DC-8	11.2	2.6	12.4	151 ± 50	0.67	226 ± 80	189 ± 84	16
23:22:31–23:31:12	DC-8	11.2	4.3	12.0	46 ± 15	0.66	70 ± 23	142 ± 70	50
23:31:20–23:36:11	DC-8	11.2	5.2	11.5	22 ± 7	0.66	33 ± 10	99 ± 56	67
23:36:30–23:44:17	DC-8	11.2	6.8	11.3	38 ± 15	0.65	59 ± 23	95 ± 53	38
Weighted mean							73 ± 12	102 ± 26	28
<i>12 June Storm^b</i>									
23:23:21–23:32:11	Falcon	10.1	6.9	11.5	179 ± 68	0.59 ^b	304 ± 128	--	--
23:34:15–23:46:19	Falcon	11.3	7.5	11.6	161 ± 65	0.66 ^b	244 ± 104	--	--
23:50:50–00:03:07	Falcon	11.9	6.4	11.6	832 ± 305	0.74 ^b	1124 ± 866	--	--
00:05:16–00:13:38	Falcon	12.3	6.8	11.5	483 ± 183	0.78 ^b	619 ± 329	--	--
Weighted mean							356 ± 88	--	--
<i>22 June Storm</i>									
23:31:09–23:43:10	G-V	11.8	8.6	13.2	148 ± 56	1.75	84 ± 33	--	--
23:46:08–23:56:05	G-V	11.2	7.9	13.1	116 ± 43	1.81	64 ± 24	--	--
23:59:05–00:10:12	G-V	10.6	8.8	12.8	40 ± 17	1.75	23 ± 9	--	--
00:12:26–00:25:43	G-V	11.5	7.8	12.8	261 ± 96	1.74	149 ± 57	--	--
00:20:34–00:35:29	DC-8	11.2	7.4	13.4	95 ± 33	1.75	54 ± 19	97 ± 46	44

Table 4. (continued)

Start/End Time (UTC)	Aircraft	Alt (km)	Anvil Cloud Base (km)	Anvil Cloud Height (km)	F_{LNO_x} (mol s^{-1})	Flash Rate (flashes s^{-1})	$P_{flux}(NO_x)^c$ (moles flash $^{-1}$)	$P_{vol}(NO_x)^d$ (moles flash $^{-1}$)	% Diff $P(NO_x)$ (vol-flux)
00:27:53–00:37:28	G-V	11.8	5.7	13.0	465 ± 158	1.76	264 ± 99	89 ± 36	66
00:35:29–00:46:04	DC-8	10.8	5.6	13.3	196 ± 66	1.75	112 ± 39	122 ± 60	8
00:51:11–01:00:38	DC-8	10.5	5.2	13.4	319 ± 106	1.70	188 ± 66	157 ± 71	16
00:58:08–01:12:09	G-V	11.2	8.5	12.6	259 ± 103	1.63	159 ± 65	99 ± 43	38
01:03:27–01:12:19	DC-8	10.9	5.0	13.1	357 ± 120	1.63	218 ± 79	283 ± 112	23
01:15:58–01:28:57	DC-8	10.9	4.5	14.2	380 ± 125	1.64	232 ± 83	179 ± 77	23
01:51:34–02:03:08	G-V	11.2	6.8	12.7	430 ± 153	1.69	254 ± 98	--	--
Weighted mean							131 ± 15	142 ± 25	8

^aAnvil estimates for the last GV transect on 16 June are not constrained by the radar or satellite data and are based solely on extrapolation of the radar cloud base and direct observation of the cloud top from GOES. Therefore, this transect has not been included in the weighted mean for the flux method.

^bDue to poor spatial overlap of this storm with the LMA, a lightning flash rate is calculated from CG flashes detected by the NLDN.

^cUncertainties in $P_{flux}(NO_x)$ determined for each transect represent the quadrature combination of uncertainties in F_{LNO_x} , the anvil depth, and the flash rate. A weighted average reported for each storm reflects the average results from the individual transects weighted by the inverse square of their fractional uncertainties.

^dResults from the volume-based approach are reported in units of moles of NO_x produced flash $^{-1}$ for direct comparison with flux-based results.

Another challenge in applying this flux-based method lies in defining the orientation and boundaries of the horizontal width (Δx) and vertical depth (Δz). Here we define this two-dimensional plane as a vertical, rectangular slice through the visible anvil cloud with the x dimension representing the direction of flight during each crosswind transect through the anvil cloud and the z dimension representing the maximum vertical depth of the anvil cloud, as depicted in Figure 2. The horizontal extent of the plane is defined using the in situ observations and is limited to when the aircraft penetrated the cloud according to the cloud data filters applied in section 2.2. Using methods outlined for volume-based calculations above, the vertical extent of the anvil is defined using radar and satellite data that are temporally and spatially coincident with each aircraft transect. Vertical limits determined from coincident radar and satellite observations that are closest in time to the midtime of each transect are reported in Table 4.

Accurate selection of the anvil depth is critical for correctly determining F_{LNO_x} . Contrasting the maximum anvil heights and minimum cloud bases determined from the combined radar and satellite observations (e.g., shaded areas in Figure S4 of the supporting information) with vertical profiles of the airborne trace gas measurements shows that anvil depths determined from the satellite-corrected radar data can be significantly larger than that determined from the vertical distribution of the in situ chemical tracers. Since the aircraft likely under sampled above and below the central part of the anvil cloud, we rely on the satellite-corrected radar data for determining the full extent of the anvil depth. One concern with using the radar data is that the detected hydrometeor-based cloud base may be lower than the true cloud base, leading to a potential overestimate of the vertical extent of the anvil. However, in-flight video from the aircraft during ascent and descents through the anvil regions indicates that these bases often occur at similar altitudes (i.e., the anvil regions are largely nonprecipitating). Here we determine uncertainties in the anvil depth by expanding the anvil cloud height and contracting the anvil cloud base by ± 500 m (i.e., the uncertainty associated with estimating the vertical extent). The resultant uncertainties for individual transects range from 10% to 56% and average 18% over all storms. Since F_{LNO_x} responds linearly with anvil depth, propagating the anvil depth uncertainties in quadrature results in uncertainties in F_{LNO_x} ranging from 31% to 63% for individual transects and an average of 37% for all storms (Table 4).

3.3. Counting Relevant Lightning Flashes

For this analysis, we define relevant lightning flashes as those flashes that contributed to the NO_x enhancements measured in each aircraft transect. We assume that NO_x is equally produced from each lightning flash regardless of flash type (e.g., IC versus CG), flash energy, and flash length

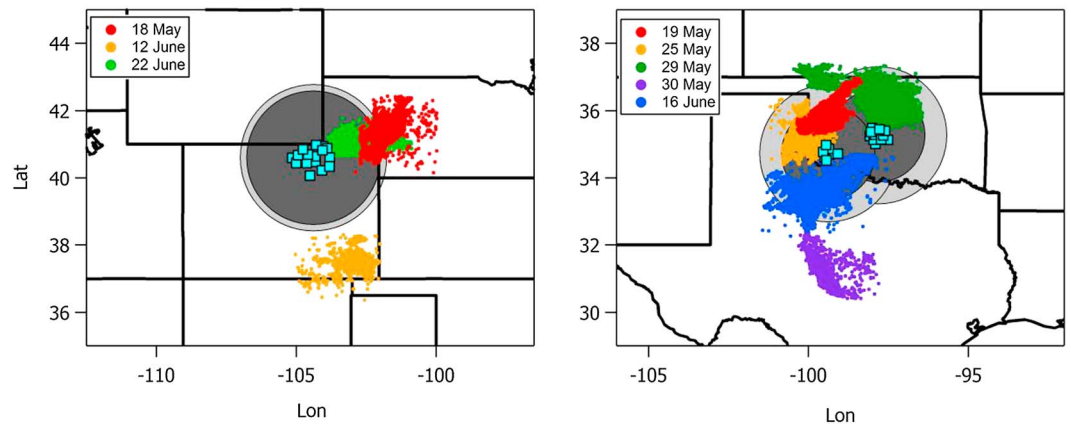


Figure 5. Locations of the individual detection stations (cyan squares) making up the (left) COLMA and (right) OKLMA networks. Lightning flashes (colored dots) from the 30 May and 12 June storms, illustrated here using the spatial locations of CG flashes detected by the NLDN, lie outside the nominal 200 km detection radius (light gray shaded circles) of each cluster. Storms, such as those on 18 and 19 May, which border the range for detecting > 95% of VHF sources per flash (dark gray shaded circles) are suspect for undercounted flashes by the LMA.

[DeCaria et al., 2000, 2005; Ridley et al., 2005; Ott et al., 2010]. Total flashes detected by the LMA are used where available for each transect. For storms sampled outside the detection radius of the LMA networks (e.g., the 30 May storm over Central Texas and 12 June storm over Southeastern Colorado shown in Figure 5), a total flash count, F_T , is calculated from the number of CG flashes (f_{CG}) detected by the NLDN and an f_{IC}/f_{CG} ratio of 4.9 for Colorado and 4.1 for northern Texas estimated from Boccippio et al. [2001] divided by a 92% detection efficiency for the Oklahoma and Texas regions of the NLDN [Biagi et al., 2007] according to equation (6).

$$F_T = \frac{[f_{CG} + f_{CG} \times (f_{IC}/f_{CG})]}{0.92} \quad (6)$$

Figure 6 illustrates a time series of the total number of relevant flashes and corresponding flash rate determined for each storm using LMA and/or NLDN observations. Flashes are counted over 5 min periods; the corresponding average flash rate in units of flashes per second is determined by dividing the number of flashes in each time bin by 300 s. Only flashes overlapping with a defined spatial and temporal window for each storm are considered relevant and thus counted. Previous observations [Lang and Rutledge, 2011; Pickering et al., 1998; Rutledge and MacGorman, 1988] that show initiation source locations for lightning flashes are coincident with storm regions with radar reflectivity > 30 dBZ. Therefore, we define the spatial limits for counting relevant flashes as the regions where flashes detected by the LMA overlap with storm radar reflectivity (e.g., the 19 May storm in Figure 7). Lightning flashes are also temporally coincident with the onset of convection; thus, we begin counting flashes when the first flash appears in the defined spatial region and stop counting when the aircraft has finished sampling each outflow transect. The total number of relevant flashes counted for each storm is reported in Table 3. As expected for these dynamic systems, the number of relevant flashes increases over time as each storm grows in size and intensity (e.g., Figure 6 and Table 3). Flash rates are calculated from the total number of relevant flashes determined for each transect divided by the elapsed time between the onset of the first flash and the time when the aircraft finished sampling that transect. Flash rates in units of flashes per second are reported in Table 4.

Increasing and decreasing the time interval for counting flashes by ± 5 min in the start and end times result in an average uncertainty of 10% in the flash count determined for each transect. Given that few flashes are counted in the early stages of storm development, uncertainties of up to 30 min (roughly 20%) in the start time have only a 1% effect on the total flash count. Therefore, significant errors in the count start time have little effect on the resulting cumulative flash count. In contrast, flash rate calculations are much more sensitive to count start time and the temporal distribution of flashes. This sensitivity is discussed further in section 4.1.

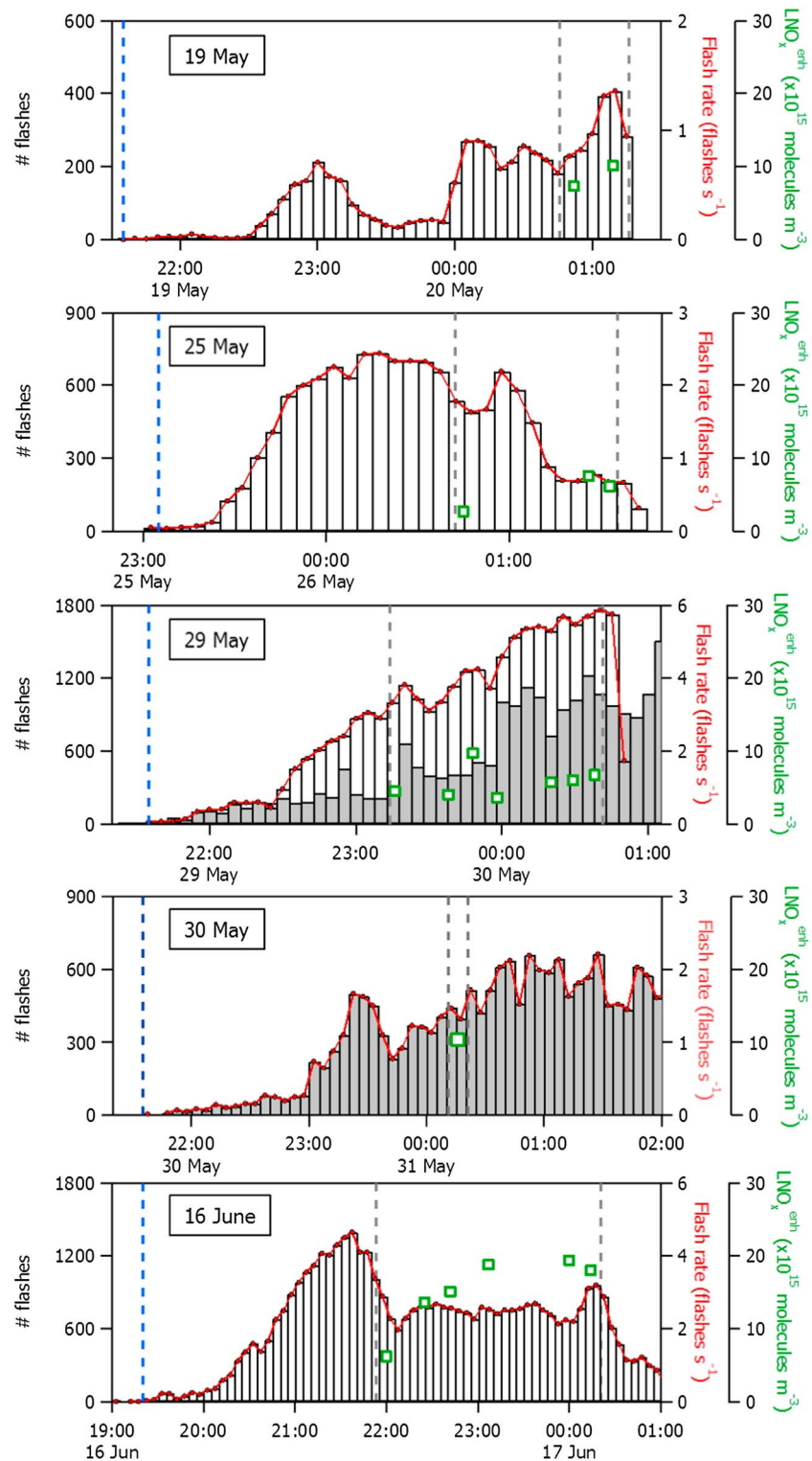


Figure 6. Time series of the total number of lightning flashes detected by the LMA (black outlined bars), or NLDN (gray shaded bars), and the corresponding flash rate (red dots) in 5 min intervals for each storm in the Oklahoma region. Gray dashed lines represent the start and end times that the aircraft were sampling each storm; blue dashed lines represent the start time for counting relevant flashes. Green symbols represent NO_x enhancements, in units of $\times 10^{15}$ molecules m^{-3} , measured during each transect.

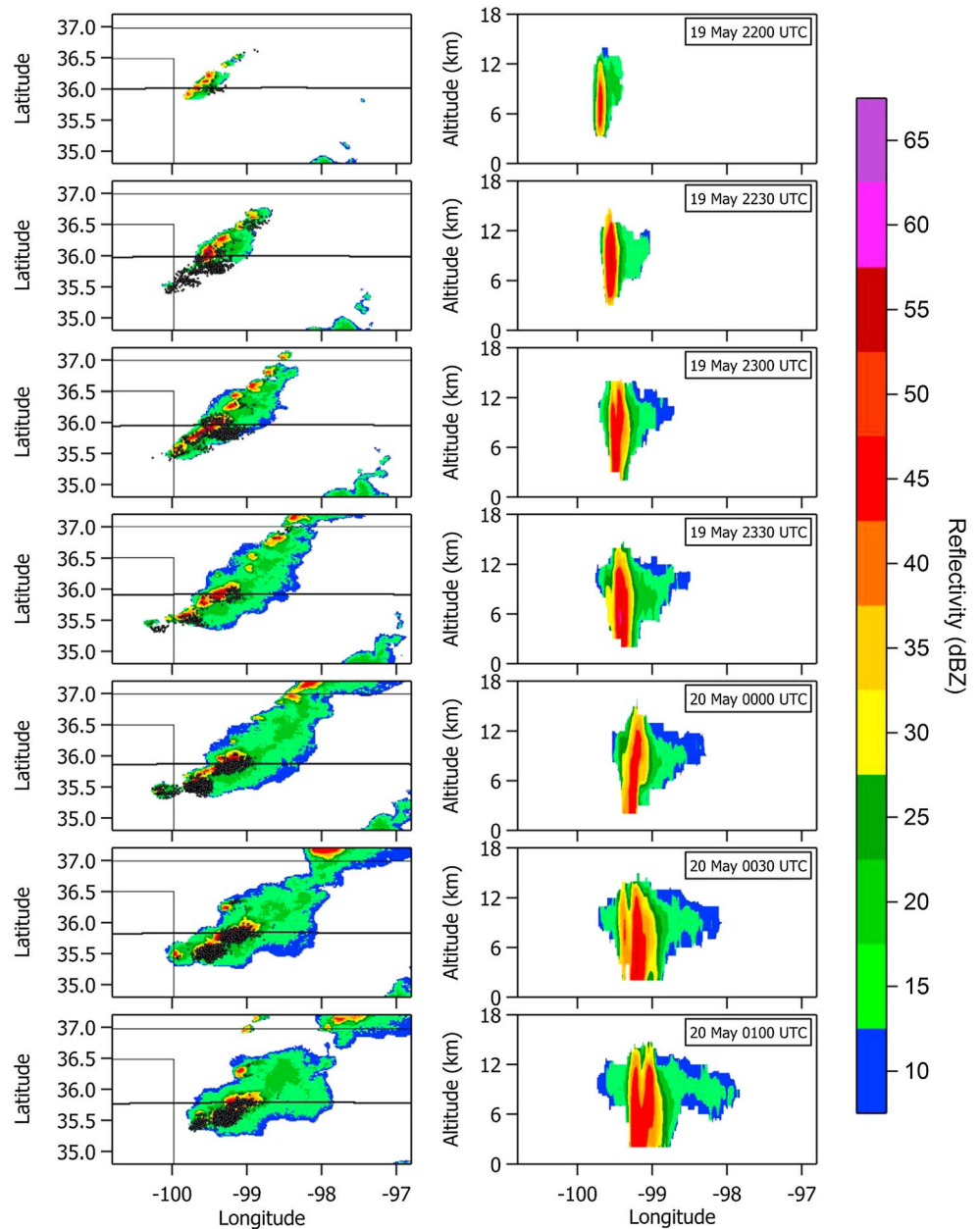


Figure 7. Time-evolved development of the 19 May storm illustrated by NEXRAD reflectivity and lightning flashes detected by the LMAs. (left) Horizontal lines (black lines) across each composite top view indicate the plane along which (right) vertical cross sections are determined. Lightning initiation source locations detected by the LMA (black symbols) overlap with regions of radar reflectivity ≥ 30 dBZ (e.g., regions with moderate precipitation).

While data from the NLDN are used to fill in the gaps for the 30 May and 12 June storms, accurate determinations of $P(\text{NO}_x)$ are subject to accurate determinations of the total flash count and flash rate using NLDN data. Comparing total flash counts determined from LMA data with total flash counts calculated from NLDN data using equation (6) for a storm with good coverage by both networks (e.g., the 29 May case in Figure 6) demonstrates that the NLDN undercounts relevant flashes by roughly 50%. The difference may be largely due to our selection of f_{IC}/f_{CG} ratio, which is simply estimated from average climatological ratios for the appropriate region reported by *Boccippio et al.* [2001]. Also, the LMAs may be detecting weaker flashes that are not detected by NLDN. However, since $P(\text{NO}_x)$ scales linearly and inversely with flash counts in this analysis, this difference suggests that $P(\text{NO}_x)$ for the 30 May and 12 June storms may be overestimated by a factor

of 2. Given additional uncertainties in the 12 June storm due to poor overlap with the radar observations and the 30 May storm due to only a single outflow transect performed by a single aircraft, we exclude these cases from further discussion and the final reported range.

We also question the total flash count, and corresponding flash rate, determined from LMA observations for two additional storms: the 18 May storm occurring near the Northeastern border of Colorado and the 19 May storm occurring near the northern border of Oklahoma. The concern is that a significant number of flashes that would have been detected closer to the network center were not counted. As the LMA detection efficiency falls off with increasing horizontal range fewer sources are detected, which makes it more challenging for clusters of VHF sources to meet the 10 source criteria to be counted as flashes. This problem is especially significant for more vigorous convection, where a larger number of flashes consist of too few VHF sources to be well detected. Undercounting the small flashes results in an overestimate of $P(\text{NO}_x)$ for these storms. Figure 5 illustrates the effect of the OKLMA and COLMA network's location and size (e.g., number of detection stations in each regional cluster) on its spatial radius for efficiently detecting VHF sources per flash. The COLMA network, which has 16 stations in a single regional cluster, is more sensitive to detecting 95% or more of the VHF sources per flash (i.e., 2σ confidence) close to the 200 km nominal detection radius. On the other hand, the OKLMA network, which is comprised of two smaller station clusters, has roughly two thirds of the nominal range for detecting 95% or more of the VHF sources making up each flash. The 18 May storm is suspected for having a large number of flashes occurring outside the network's nominal detection range (e.g., half of the lightning flashes are located outside the shaded circles in Figure 5), while the 19 May case is suspected for having flashes consisting of too few VHF sources to be detected at the 200 km limit of the nominal detection range. Although careful assessment of the detection efficiency for each network is outside the scope of this analysis, we assume that most of the lightning flashes associated with the six DC3 storms considered here had enough VHF sources per flash to be well detected by the LMA. Therefore, without further detailed information, we have no basis for eliminating these two storms from subsequent analyses and discussion.

3.4. Resulting NO_x Production Flash⁻¹

Tables 3 and 4 report the resultant molecules (or moles) of NO_x produced flash⁻¹ for each storm using the volume-based, $P_{\text{vol}}(\text{NO}_x)$, and flux-based, $P_{\text{flux}}(\text{NO}_x)$, approaches. $P_{\text{vol}}(\text{NO}_x)$ is determined by dividing $N_{\text{vol}}(\text{NO}_x)$, in units of molecules (or moles) from equation (4), by the corresponding number of relevant lightning flashes. $P_{\text{flux}}(\text{NO}_x)$ is determined by dividing F_{LNO_x} , in units of mol s^{-1} from equation (5), by the corresponding average flash rate in units of flashes per second. Considering the results from both approaches for the six retained storms, $P(\text{NO}_x)$ ranges from 73 to 437 $\text{mol NO}_x \text{ flash}^{-1}$ and is reduced to 84–291 $\text{mol NO}_x \text{ flash}^{-1}$ without the 18 May and 19 May storms and the low-biased $P_{\text{vol}}(\text{NO}_x)$ value for the 29 May storm. The storm-to-storm variability is much larger than the total uncertainty for quantifying $P(\text{NO}_x)$ from each storm. Propagating the uncertainties in quadrature results in a total average uncertainty of 40% for $P(\text{NO}_x)$ using either approach. Similarities in the final average uncertainties determined for each approach reflect contributions from common terms in equations (4) and (5) (e.g., an average uncertainty of 33% for measuring NO_x enhancements in the outflow, an average uncertainty of 15% for storm volume and 18% for anvil depth, and an average uncertainty of 10% for determining the relevant lightning flash count or flash rate). Propagating the uncertainties for $P(\text{NO}_x)$ from each of the six storms in this analysis results in an all-inclusive, measurement-based range of 60 to 570 $\text{mol NO}_x \text{ flash}^{-1}$ (or 65–332 $\text{mol NO}_x \text{ flash}^{-1}$ without the suspect storms).

4. Discussion

4.1. Volume-Based Versus Flux-Based Approaches

Moles of $\text{NO}_x \text{ flash}^{-1}$ resulting from the volume-based and flux-based approaches are compared in Table 4. The volume-based approach results in values for $P_{\text{vol}}(\text{NO}_x)$ from six storms ranging from 102 to 437 $\text{mol NO}_x \text{ flash}^{-1}$, with an average of 205 $\text{mol NO}_x \text{ flash}^{-1}$. The range is reduced to 142–291 $\text{mol NO}_x \text{ flash}^{-1}$ and average to 194 $\text{mol NO}_x \text{ flash}^{-1}$ after excluding the 18 May and 19 May storms and the low-biased $P_{\text{vol}}(\text{NO}_x)$ value from 29 May. The flux-based approach results in values for $P_{\text{flux}}(\text{NO}_x)$ ranging from 73 to 407 $\text{mol NO}_x \text{ flash}^{-1}$ (or 84–205 without the 18 and 19 May storms), with an average of 174 (or 140) moles of $\text{NO}_x \text{ flash}^{-1}$. Results from the two methods are similar, with differences largely encompassed by the reported 1σ uncertainties for

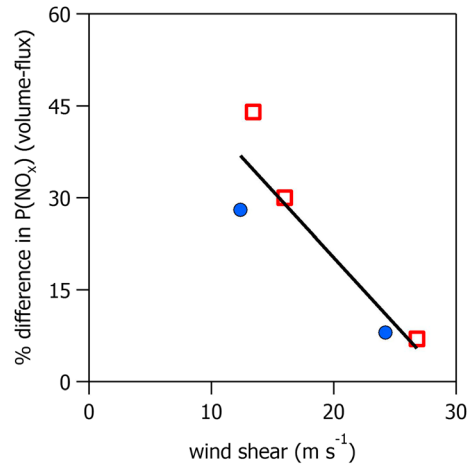


Figure 8. Scatterplot of the percent difference between $P_{vol}(NO_x)$ and $P_{flux}(NO_x)$ from Table 4 versus vertical wind shear from Table 1 for all storms sampled in the Oklahoma (red squares) and Colorado (blue circles) regions except the storm on 29 May. Linear regression (solid black line) shows strong correlation ($r^2 = 0.82$) between percent difference and wind shear.

each individual transect. With the exception of the 29 May storm, the volume-based approach consistently results in greater values for $P(NO_x)$ (e.g., values for $P_{vol}(NO_x)$ that are 7 to 44% larger than values for $P_{flux}(NO_x)$). Figure 8 depicts a scatterplot of the percent differences between $P_{vol}(NO_x)$ and $P_{flux}(NO_x)$ for each storm versus vertical wind shear. Linear regression of the data points for all storms except 29 May shows strong correlation ($r^2 = 0.82$) between the differences in $P(NO_x)$ and vertical wind shear suggesting that the physical characteristics of each storm may play an important role in determining the best method of analysis. For example, if the storm is well isolated and there are strong enough winds aloft to horizontally stretch the outflow in the downwind direction, then both methods should produce similar results for $P_{vol}(NO_x)$ and $P_{flux}(NO_x)$. This is the case for the storms on 19 May and 22 June, where vertical wind shear exceeds 20 m s^{-1} . In contrast, it is more difficult to capture LNO_x enhancements using the flux-based approach for storms with more circular anvils, such as those on 18 May, 25 May, and 16 June with vertical wind shears of $\leq 16 \text{ m s}^{-1}$. Accurate application of the flux-based method requires that lightning, and hence production of NO, occurs

far enough upwind of the two-dimensional flux plane for LNO_x^{enh} to be sampled by the aircraft. Therefore, the volume-based method may generate more reliable results for isolated storms with less vertical shear.

Along the same reasoning, the flux-based approach may also be more sensitive to our criteria for selecting relevant flashes. Ideally, only the lightning flashes with initiation sources located upwind of the flux plane (i.e., outflow transects performed by the aircraft) ought to be considered for the flux-based analysis. While overlaying the LMA initiation sources and aircraft flight path shows that nearly all of the lightning flashes occurred upwind of the aircraft transects (e.g., the 29 May storm in Figure 9), it is possible that NO_x produced by lightning flashes occurring spatially close to the flux plane or at the temporal onset of the storm may have passed downwind of the flux plane prior to sampling by the aircraft. This is of particular concern for flashes with initiation source locations spatially close to each transect since the majority of the lightning channel may have occurred downwind of the transect. While a time-evolved model of the LNO_x trajectories from each flash with respect to the flux plane is beyond the scope of this work, we can test the sensitivity of the flux-based

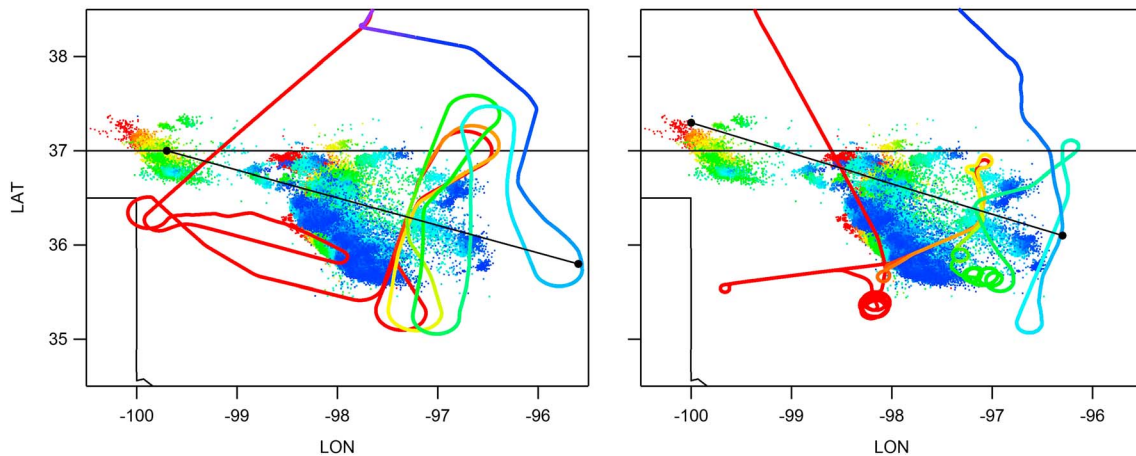


Figure 9. Flight tracks (lines) and flash initiation source locations detected by the LMA (dots) for the 29 May storm. Flight tracks from the (left) G-V aircraft and (right) DC-8 and relevant flashes are colored by the same timescale, with warm colors being earlier and cool colors being later. The origin and trajectory of the air mass sampled during the final transect performed by each aircraft, determined using wind speed and wind direction during the final transect, is depicted as a solid black line.

calculations to our selection of the start time for counting relevant flashes by comparing the location of flashes occurring at the onset of the storm with the spatial origin of the air mass sampled by the aircraft during each transect. Here we determine the origin of the air mass from the position, wind speed, and wind direction measured by the aircraft during each transect. Figure 9 illustrates that the origin of the air mass sampled during aircraft transects from the 29 May storm overlaps with lightning flashes occurring at the onset of the storm.

Further, the $P_{\text{flux}}(\text{NO}_x)$ values reported in Table 4 may be sensitive to the assumptions required to apply the flux-based calculations to DC3 cases. For example, neglecting the effect of storm motion in the flux-based approach, which may play a small role in some DC3 cases, likely results in larger values for $P_{\text{flux}}(\text{NO}_x)$ than those reported in Table 4. On the other hand, the flux-based results have the opposite sensitivity to the amount of data available for the calculation. Despite the advantage of the flux-based approach to account for the horizontal distribution of NO_x in comparison to the volume-based approach, time gaps in the NO_x measurements exceeding the 1 s timescale used for instantaneous flux calculations undoubtedly lead to unquantifiable underestimates in $\text{LNO}_x^{\text{enh}}$ and consequently $P_{\text{flux}}(\text{NO}_x)$. Since quantifying the sensitivity of $P_{\text{flux}}(\text{NO}_x)$ in either of these scenarios is beyond the scope of this work, $P_{\text{flux}}(\text{NO}_x)$ values in Table 4 cannot be reported as upper or lower limits.

4.2. Consideration of Lightning Flash Characteristics

Previous studies [Borucki and Chameides, 1984; Price et al., 1997a, 1997b; Stith et al., 1999; Wang et al., 1998; Huntrieser et al., 2008] have considered whether CG lightning flashes, flashes with greater energy (e.g., flashes with a higher multiplicity or a larger number of strokes), and flashes with greater extent (e.g., longer length or larger area) produce more NO_x . We start by considering NO_x production as a function of flash type. Previous studies [Gallardo and Cooray, 1996; Price et al., 1997a; Bond et al., 2001] suggested that IC flashes could produce as much as 10 times less NO_x than CG flashes (i.e., a productivity ratio of 0.1). More recent analyses of airborne lightning observations with cloud model simulations [DeCaria et al., 2000, 2005; Fehr et al., 2004; Ridley et al., 2005] indicate that IC flashes produce about the same amount of NO_x as CG flashes (i.e., a productivity ratio of 1), thereby suggesting that equal NO_x production per flash is a reasonable assumption for our analysis. Nevertheless, we demonstrate the sensitivity of $P(\text{NO}_x)$ to NO_x productivity per type of flash by calculating that $P(\text{NO}_x)$ for storms in the Oklahoma and Colorado regions would be 72% and 75% less than the respective values reported in Table 4 if IC flashes produce 10 times less NO_x than CG flashes (calculations shown in the supporting information).

Huntrieser et al. [2008] and Stith et al. [1999] have suggested that flashes with a longer spatial length produce more NO_x . Thus, we also consider NO_x production as a function of the flash area. Here we calculate the sum of all flash areas (in 2 min intervals), where the sum is proportional to the total flash energy [Bruning and Thomas, 2015, Appendix C]. A cumulative flash area, in units of square kilometers, is determined for the relevant time period of each storm and represents the sum of the flash areas from the onset of lightning (blue dashed line in Figure 6) until the departure of the aircraft from the storm (second gray dashed line in Figure 6). A scatterplot of $P(\text{NO}_x)$ versus the cumulative flash area (e.g., Figure 10) indicates a possible positive correlation between moles of $\text{NO}_x \text{ flash}^{-1}$ and the average flash area observed in each storm suggesting some plausibility to this hypothesis; however, linear regression of the data points weighted by the inverse square of the reported uncertainties returns values for $r^2 < 0.08$. Eliminating the suspect storms on 18 and 19 May and $P_{\text{vol}}(\text{NO}_x)$ from the 29 May storm prior to linear regression results in a similar positive trend and increases the correlation coefficient to 0.22. Future works may improve upon these possible correlations as additional flash energy and flash length data products are analyzed from the DC3 LMA data set.

4.3. Comparison With Storm Kinematic Properties

Connecting $P(\text{NO}_x)$ to storm kinematic properties, such as wind shear, is also of interest as these properties are easily determined in forecast and climate models. In addition, the wind shear is a factor in determining the lightning flash rate and flash extent. Huntrieser et al. [2008] discussed whether there is positive correlation between $P(\text{NO}_x)$ and vertical wind shear. A large vertical storm shear is expected to elongate the anvil cloud such that flashes with longer lengths may be dominant. By association if LNO_x production increases with increasing flash length, then we could expect increases in $P(\text{NO}_x)$ with increases in wind shear. A scatterplot of our resultant values for $P(\text{NO}_x)$ versus wind shear (e.g., Figure 10) indicates a possible positive correlation; however, linear regression of the data points weighted by the inverse square of the reported uncertainties

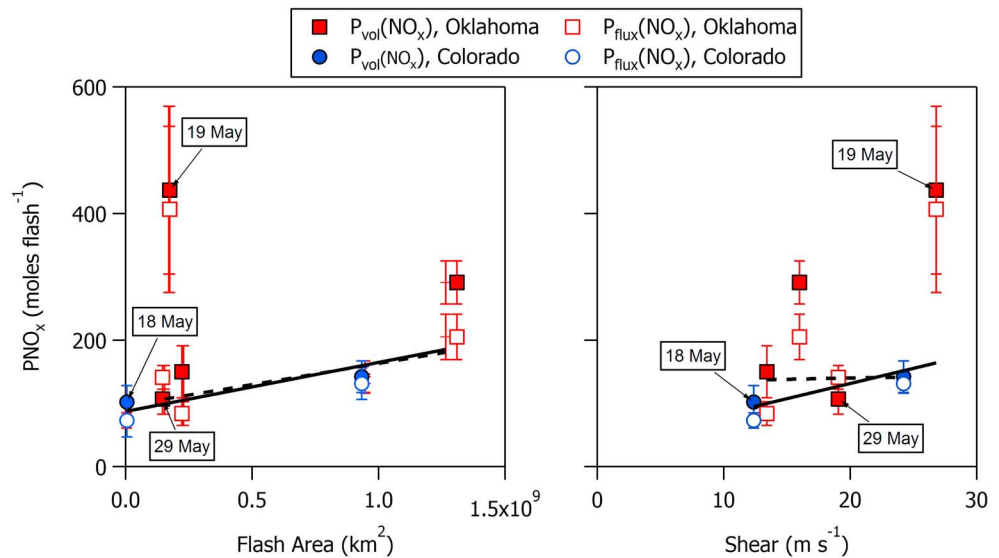


Figure 10. Scatterplot of $P_{vol}(NO_x)$ (closed symbols) and $P_{flux}(NO_x)$ (open symbols) versus (left) cumulative flash area and (right) vertical wind shear. Linear regression weighted by the inverse square of the 1σ propagated uncertainties (solid black lines) suggests positive correlations for $P(NO_x)$ versus flash area ($r^2 < 0.08$) and $P(NO_x)$ versus wind shear ($r^2 < 0.04$). Eliminating the suspect storms on 18 and 19 May and $P_{vol}(NO_x)$ from 29 May (dashed black line) results in a stronger correlation ($r^2 = 0.22$) between $P(NO_x)$ and flash area but no distinct correlation for $P(NO_x)$ versus wind shear.

returns an $r^2 < 0.04$. Eliminating the suspect storms on 18 and 19 May and $P_{vol}(NO_x)$ from 29 May further indicates no distinct correlation.

4.4. Comparison With Regional and Global Values

Previous reports have shown significant differences in lightning frequency for different geographical regions [Bocchippio *et al.*, 2001]. For example, in the U.S., lightning frequency generally decreases across the mainland from the southeast to the northwest with the highest frequency of cloud-to-ground lightning occurring in regions with large atmospheric moisture content and high surface temperatures that produce strong sea breezes, such as Florida and along the Gulf of Mexico and Atlantic coasts. Strong upward motions also contribute to frequent cloud-to-ground lightning in the western mountains; the least cloud-to-ground lightning is observed along the Pacific west coast. For geographical perspective, using values reported in Schumann and Huntrieser [2007], $P(NO_x)$ ranges from 66 to 1328 mol NO_x flash⁻¹ for storms located in northern latitudes such as Germany, Illinois, and Saskatchewan, while $P(NO_x)$ ranges from 31 to 814 mol NO_x flash⁻¹ for storms sampled in tropical and subtropical coastal environments such as Northern Australia, Western India, Brazil, Africa, the Gulf of Mexico, and Florida. Therefore, we compare our region-specific $P(NO_x)$ values with values previously reported for storms sampled over the U.S. Great Plains (e.g., Table 5) rather than the global range reported by Schumann and Huntrieser [2007].

$P(NO_x)$ values from analyses of storms over Colorado and New Mexico dating back to 1976 range from 21 to 1444 mol NO_x flash⁻¹. This range includes results from a combination of measurement-based analyses and modeling studies. Noxon [1976] reported the first field-based measurements of $P(NO_x)$ over Colorado. Results were reported in units of moles of NO_2 produced per flash and consisted of analyses of ground-based NO_2 absorption spectroscopy measurements combined with estimates of lightning flash rates from visible observations. Ridley *et al.* [1996] determined moles of NO_x produced per flash in storms sampled over New Mexico in 1989; the study combined airborne measurements of NO_x with ground-based measurements of CG lightning flashes. The latter was adjusted for total flashes using an f_{IC}/f_{CG} ratio estimated from ground-based measurements made with electric field change meters. Subsequent studies over Colorado, such as STERAO in 1996 [Stith *et al.*, 1999], determined moles of NO produced per flash using airborne measurements of NO and NO_x combined with ground-based observations of lightning flashes using the French Office National d'Etudes et de Recherches Aérospatiales (ONERA) three-dimensional VHF interferometer. More

Table 5. $P(\text{NO}_x)$, in Units of Moles Flash⁻¹, Reported for Storms Sampled Over the U.S. Great Plains Since 1976

Year	Study	Location	$P(\text{NO}_x)$	Method	Reference
1976		Colorado	166 ^a	Ground-based NO ₂ absorption spectroscopy	Noxon [1976]
1989	ELCHEM	New Mexico	47–60	In situ ground-based and airborne observations	Ridley et al. [1996]
1996	STERAO	Colorado	21–208 ^b	In situ ground-based and airborne observations	Stith et al. [1999]
1996	STERAO	Colorado	232–465	Modeled estimate based on field observations	DeCaria et al. [2000]
1996	STERAO	Colorado	43	Modeled estimate based on airborne observations	Skamarock et al. [2003]
1996	STERAO	Colorado	345–460	Modeled estimate based on field observations	DeCaria et al. [2005]
1996	STERAO	Colorado	195–390	Modeled estimate based on field observations	Barth et al. [2007]
1996	STERAO	Colorado	37	Modeled estimate based on field observations	Barthe et al. [2007]
1996	STERAO	Colorado	121	Modeled estimate based on field observations	Barthe and Barth [2008]
1996	STERAO	Colorado	234–390	Modeled estimate based on field observations	Ott et al. [2010]
2002		Colorado	481–1444 ^c	Ground-based absorption spectroscopy	Langford et al. [2004]
2012	DC3	Colorado	73–142	In situ ground-based and airborne observations	This work
2012	DC3	Oklahoma	84–437	In situ ground-based and airborne observations	This work
		Global	32–664	Synthesis of measured and modeled analyses between 1976 and 2007	Schumann and Huntrieser [2007]

^aReported values are in units of moles of NO₂ per flash and use flash rates estimated from visible observations.

^bValues adapted from Stith et al. [1999] by Schumann and Huntrieser [2007] and reported in units of moles of NO per flash. Calculations utilize the number of flashes detected by the French Office National d'Etudes et de Recherches Aéropatiales (ONERA) three-dimensional VHF interferometer.

^cReported values are in units of moles of NO₂ per CG flash and use the number of CG flashes detected by the NLDN.

recently, Langford et al. [2004] used absorption spectroscopy to quantify moles of NO₂ per CG flash detected by the NLDN for a single storm over Boulder, Colorado. Modeled estimates involve analyses based on field observations from STERAO and include values reported by DeCaria et al. [2000, 2005], Skamarock et al. [2003], Barth et al. [2007], Barthe et al. [2007], and Barthe and Barth [2008]. Although a large range of results was expected given the inherent variability in storms and that these analyses often relied on a single storm or lightning flash event, differences in the results reported in Table 5 span 2 orders of magnitude. These differences may largely be attributed to differences in the lightning detection network data set used for the analysis and whether total flashes versus only CG flashes were considered. As shown above in section 3.3, total flash counts based on NLDN data are severely underestimated in comparison to the LMA data leading to overestimates in $P(\text{NO}_x)$ as large as a factor of 2, while analyses solely using CG flash counts can lead to overestimates for the Great Plains region larger than a factor of 5. Excluding the values reported by Langford et al. [2004], which represent moles produced per CG flash rather than total (IC + CG) flashes, from the historical assessments reduces the range in $P(\text{NO}_x)$ for the Great Plains to 21–465 mol NO_x flash⁻¹. Our results from six DC3 storms suggest an increase in the lower limit of this range to 73 mol NO_x flash⁻¹, or 60 mol NO_x flash⁻¹ when including uncertainties, and indicate no reduction in the upper limit (e.g., 437 mol NO_x flash⁻¹ or 570 mol NO_x flash⁻¹ when uncertainties are included). However, excluding the questionable values for the storms on 18, 19, and 29 May and solely utilizing results from the more robust volume-based approach constrain the lower limit to 142 and upper limit to 291 mol NO_x flash⁻¹ (or 117–332 mol NO_x flash⁻¹ when uncertainties are included).

5. Summary

In this study, a measurement-based range for molecules (or moles) of NO_x produced per lightning flash is quantified using in situ airborne and ground-based measurements collected for six isolated thunderstorms occurring near Oklahoma and Colorado during the DC3 experiment. Two approaches for converting LNO_x enhancements from volume-based mixing ratios to molecules of NO_x (i.e., the volume-based approach) or a mass flux of NO_x in units of mol s⁻¹ (i.e., the flux-based approach) are evaluated using the common data set of DC3 observations. Results for the six storms using the volume-based approach, $P_{\text{vol}}(\text{NO}_x)$, range from 102 to 437 mol of NO_x flash⁻¹ with an average of 205 mol of NO_x flash⁻¹, and results from the flux-based approach, $P_{\text{flux}}(\text{NO}_x)$, range from 73 to 407 mol of NO_x flash⁻¹ with an average of 173 mol of NO_x flash⁻¹. On a per storm basis, $P(\text{NO}_x)$ values resulting from the volume-based method are consistently larger than those from the flux-based method with percent differences between $P_{\text{vol}}(\text{NO}_x)$ and $P_{\text{flux}}(\text{NO}_x)$ ranging from 7 to 44%. Storms with asymmetric, elongated anvils (e.g., greater vertical wind shear) tend to produce smaller percent differences between the two methods, while storms with a more circular-shaped anvil (e.g., less vertical wind shear) produce results with larger percent differences. Owing to this difference and to the

significant dependence of the flux-based method on the strength of the flow normal to the aircraft, we conclude that the volume-based approach generates more reliable results for storms with less vertical shear. Weak positive correlations between $P(\text{NO}_x)$ and vertical wind shear and flash area also suggest a possible increase in NO_x production per flash in storms with increasingly elongated anvils (e.g., longer IC flash lengths). While the combined results from both methods and including uncertainties for the six DC3 storms sampled over Oklahoma and Colorado fail to significantly constrain the previously reported range for storms occurring in the Great Plains, exclusion of questionable values for the storms on 18, 19, and 29 May and solely using results from the volume-based approach suggest that the lower and upper limits may be closer to 142 and 291 mol NO_x flash⁻¹, respectively.

Acknowledgments

The Deep Convective Clouds and Chemistry (DC3) experiment is sponsored by the U.S. National Science Foundation (NSF), the National Aeronautics and Space Administration (NASA), the National Oceanic and Atmospheric Administration (NOAA), and the Deutsches Zentrum fuer Luft- und Raumfahrt (DLR). Archived field data can be accessed from <http://data.eol.ucar.edu/> or <http://www-air.larc.nasa.gov/cgi-bin/ArcView/dc3-seac4rs>. NLDN data are collected by Vaisala, Inc. and archived at NASA Marshall Space Flight Center for NASA-related Earth Science research. Data provided by NCAR/EOL are supported by the National Science Foundation. Support for NOAA chemiluminescence-based measurements of O_3 , NO , NO_2 , and NO_x aboard the NASA DC-8 during DC3 comes from NASA grant NNH12AT301. Acetone/propanal measurements aboard the DC-8 during DC3 were supported by the Austrian Federal Ministry for Transport, Innovation, and Technology (BMVIT) through the Austrian Space Applications Programme (ASAP) of the Austrian Research Promotion Agency (FFG). The authors acknowledge R.C. Cohen and B. Nault (University of California, Berkeley) for TD-LIF NO_2 measurements aboard the DC-8 aircraft, O. Cooper (NOAA) for digested images from the GOES satellite, SPEC Inc. for cloud probe measurements aboard the DC-8, K. Froyd (NOAA) and M. Markovic (Environment Canada) for providing a visual-based cloud indicator for DC-8 flights, A. Minikin and D. Fuetterer (DLR) for providing cloud probe data from the Falcon aircraft, and J. Jensen and J. Stith (NCAR/EOL) for cloud data products from the G-V. The authors appreciate discussions with S.A. Rutledge, B. Fuchs, and B. Basarab (Colorado State University) and helpful comments on the manuscript from B.A. Ridley (NCAR-emeritus) and M. Trainer (NOAA).

References

- Apel, E. C., et al. (2015), Upper tropospheric ozone production from lightning NO_x -impacted convection: Smoke ingestion case study from the DC3 campaign, *J. Geophys. Res. Atmos.*, *120*, 2505–2523, doi:10.1002/2014JD022121.
- Baehr, J., H. Schlager, H. Ziereis, P. Stock, P. van Velthoven, R. Busen, J. Ström, and U. Schumann (2003), Aircraft observations of NO , NO_y , CO , and O_3 in the upper troposphere from 60°N to 60°S—Interhemispheric differences at midlatitudes, *Geophys. Res. Lett.*, *30*(11), 1598, doi:10.1029/2003GL016935.
- Barth, M. C., S.-W. Kim, W. C. Skamarock, A. L. Stuart, K. E. Pickering, and L. E. Ott (2007), Simulations of the redistribution of formaldehyde, formic acid, and peroxides in the 10 July 1996 Stratospheric-Tropospheric Experiment: Radiation, Aerosols, and Ozone deep convection storm, *J. Geophys. Res.*, *112*, D13310, doi:10.1029/2006JD008046.
- Barth, M. C., J. Lee, A. Hodzic, G. Pfister, W. C. Skamarock, J. Worden, J. Wong, and D. Noone (2012), Thunderstorms and upper troposphere chemistry during the early stages of the 2006 North American Monsoon, *Atmos. Chem. Phys.*, *12*, 11,003–11,026, doi:10.5194/acp-12-11003-2012.
- Barth, M. C., et al. (2015), The Deep Convective Clouds and Chemistry (DC3) field campaign, *Bull. Am. Meteorol. Soc.*, doi:10.1175/BAMS-D-13-00290.1.
- Barthe, C., and M. C. Barth (2008), Evaluation of a new lightning-produced $\text{NO}(x)$ parameterization for cloud resolving models and its associated uncertainties, *Atmos. Chem. Phys.*, *8*(16), 4691–4710.
- Barthe, C., J.-P. Pinty, and C. Mari (2007), Lightning-produced NO_x in an explicit electrical scheme tested in a Stratosphere-Troposphere Experiment: Radiation, Aerosols, and Ozone case study, *J. Geophys. Res.*, *112*, D04302, doi:10.1029/2006JD007402.
- Biagi, C. J., K. L. Cummins, K. E. Kehoe, and E. P. Krider (2007), National Lightning Detection Network (NLDN) performance in southern Arizona, Texas, and Oklahoma in 2003–2004, *J. Geophys. Res.*, *112*, D05208, doi:10.1029/2006JD007341.
- Boccippio, D. J., S. J. Goodman, and S. Heckman (2001), Regional differences in tropical lightning distributions, *J. Appl. Meteorol.*, *39*(12), 2231–2248, doi:10.1175/1520-0450(2001)040<2231:Rditld>2.0.Co;2.
- Boggs, P. T., R. H. Byrd, and R. B. Schnabel (1987), A stable and efficient algorithm for nonlinear orthogonal distance regression, *SIAM J. Sci. Comput.*, *8*, 1052–1078.
- Bond, D. W., R. Zhang, X. Tie, G. Brasseur, G. Huffines, R. E. Orville, and D. J. Boccippio (2001), NO_x production by lightning over the continental United States, *J. Geophys. Res.*, *106*, 27,701–27,710, doi:10.1029/2000JD000191.
- Borucki, W. J., and W. L. Chameides (1984), Lightning—Estimates of the rates of energy-dissipation and nitrogen-fixation, *Rev. Geophys.*, *22*, 363–372, doi:10.1029/RG022i004p0363.
- Bruning, E. C., and D. R. MacGorman (2013), Theory and observations of controls on lightning flash size spectra, *J. Atmos. Sci.*, *70*, 4012–4029, doi:10.1175/JAS-D-12-0289.1.
- Bruning, E. C., and R. J. Thomas (2015), Lightning channel length and flash energy determined from moments of the flash area distribution, *J. Geophys. Res. Atmos.*, *120*, 8925–8940, doi:10.1002/2015JD023766.
- Chameides, W. L. (1979), Effect of variable energy input of nitrogen fixation in instantaneous linear discharges, *Nature*, *277*, 123–124.
- Chameides, W. L., D. H. Stedman, R. R. Dickerson, D. W. Rusch, and R. J. Cicerone (1977), NO_x production in lightning, *J. Atmos. Sci.*, *34*(1), 143–149, doi:10.1175/1520-0469(1977)034<0143:Npil>2.0.Co;2.
- Chameides, W. L., D. D. Davis, J. Bradshaw, M. Rodgers, S. Sandholm, and D. B. Bai (1987), An estimate of the NO_x production-rate in electrified clouds based on NO observations from the GTE/CITE-1 fall 1983 field operation, *J. Geophys. Res.*, *92*, 2153–2156, doi:10.1029/JD092iD02p02153.
- Chen, H., et al. (2010), High-accuracy continuous airborne measurements of greenhouse gases (CO_2 and CH_4) using the cavity ring-down spectroscopy (CRDS) technique, *Atmos. Meas. Tech.*, *3*(2), 375–386, doi:10.5194/amt-3-375-2010.
- Crum, T. D., and R. L. Albery (1993), The WSR-88D and the WSR-88D operational support facility, *Bull. Am. Meteorol. Soc.*, *74*(9), 1669–1687.
- DeCaria, A. J., K. E. Pickering, G. L. Stenchikov, J. R. Scala, J. L. Stith, J. E. Dye, B. A. Ridley, and P. Laroche (2000), A cloud-scale model study of lightning-generated NO_x in an individual thunderstorm during STERAO-A, *J. Geophys. Res.*, *105*, 11,601–11,616, doi:10.1029/2000JD900033.
- DeCaria, A. J., K. E. Pickering, G. L. Stenchikov, and L. E. Ott (2005), Lightning-generated NO_x and its impact on tropospheric ozone production: A three-dimensional modeling study of a Stratosphere-Troposphere Experiment: Radiation, Aerosols and Ozone (STERAO-A) thunderstorm, *J. Geophys. Res.*, *110*, D14303, doi:10.1029/2004JD005556.
- de Gouw, J., and C. Warneke (2007), Measurements of volatile organic compounds in the Earth's atmosphere using proton-transfer-reaction mass spectrometry, *Mass Spectrom. Rev.*, *26*, 223–257, doi:10.1002/mas.20119.
- Dye, J. E., et al. (2000), An overview of the Stratospheric-Tropospheric Experiment: Radiation, Aerosols, and Ozone (STERAO)-Deep Convection experiment with results for the July 10, 1996 storm, *J. Geophys. Res.*, *105*, 10,023–10,045, doi:10.1029/1999JD901116.
- Fehr, T., H. Höller, and H. Huntrieser (2004), Model study on production and transport of lightning-produced NO_x in a EULINOX supercell storm, *J. Geophys. Res.*, *109*, D09102, doi:10.1029/2003JD003935.
- Gallardo, L., and V. Cooray (1996), Could cloud-to-cloud discharges be as effective as cloud-to-ground discharges in producing NO_x ?, *Tellus, Ser. B*, *48*(5), 641–651, doi:10.1034/j.1600-0889.1996.t01-4-00003.x.
- Gerbig, C., S. Schmitgen, D. Kley, A. Volz-Thomas, K. Dewey, and D. Haaks (1999), An improved fast-response vacuum-UV resonance fluorescence CO instrument, *J. Geophys. Res.*, *104*, 1699–1704.

- Homeyer, C. R. (2014), Formation of the enhanced-V infrared cloud top feature from high-resolution three-dimensional radar observations, *J. Atmos. Sci.*, *71*(1), 332–348, doi:10.1175/JAS-D-13-079.1.
- Homeyer, C. R., and M. R. Kumjian (2015), Microphysical characteristics of overshooting convection from polarimetric radar observations, *J. Atmos. Sci.*, *72*(2), 870–891, doi:10.1175/JAS-D-13-0388.1.
- Huntrieser, H., H. Schlager, C. Feigl, and H. Höller (1998), Transport and production of NO_x in electrified thunderstorms: Survey of previous studies and new observations at midlatitudes, *J. Geophys. Res.*, *103*, 28,247–28,264, doi:10.1029/98jd02353.
- Huntrieser, H., et al. (2002), Airborne measurements of NO_x, tracer species, and small particles during the European lightning nitrogen oxides experiment, *J. Geophys. Res.*, *107*(D11), 4113, doi:10.1029/2000JD000209.
- Huntrieser, H., U. Schumann, H. Schlager, H. Höller, A. Giez, H.-D. Betz, D. Brunner, C. Forster, O. Pinto Jr., and R. Calheiros (2008), Lightning activity in Brazilian thunderstorms during TROCCINOX: Implications for NO(x) production, *Atmos. Chem. Phys.*, *8*(4), 921–953.
- Huntrieser, H., et al. (2009), NO_x production by lightning in Hector: First airborne measurements during SCOUT-O3/ACTIVE, *Atmos. Chem. Phys.*, *9*(21), 8377–8412, doi:10.5194/acp-9-8377-2009.
- Huntrieser, H., H. Schlager, M. Lichtenstern, P. Stock, T. Hamburger, H. Höller, K. Schmidt, H.-D. Betz, A. Ulanovsky, and F. Ravegnani (2011), Mesoscale convective systems observed during AMMA and their impact on the NO_x and O₃ budget over West Africa, *Atmos. Chem. Phys.*, *11*(6), 2503–2536, doi:10.5194/acp-11-2503-2011.
- Lamarque, J.-F., G. P. Brasseur, P. G. Hess, and J.-F. Müller (1996), Three-dimensional study of the relative contributions of the different nitrogen sources in the troposphere, *J. Geophys. Res.*, *101*(D17), 22,955–22,968, doi:10.1029/96JD02160.
- Lang, T. J., and S. A. Rutledge (2011), A framework for the statistical analysis of large radar and lightning datasets: Results from STEPS 2000, *Mon. Weather Rev.*, *139*(8), 2536–2551, doi:10.1175/Mwr-D-10-05000.1.
- Langford, A. O., R. W. Portmann, J. S. Daniel, H. L. Miller, and S. Solomon (2004), Spectroscopic measurements of NO₂ in a Colorado thunderstorm: Determination of the mean production by cloud-to-ground lightning flashes, *J. Geophys. Res.*, *109*, D11304, doi:10.1029/2003JD004158.
- Li, Q. B., D. J. Jacob, J. W. Munger, R. M. Yantosca, and D. D. Parrish (2004), Export of NO_y from the North American boundary layer: Reconciling aircraft observations and global model budgets, *J. Geophys. Res.*, *109*, D02313, doi:10.1029/2003JD004086.
- Lund, N. R., D. R. MacGorman, T. J. Schuur, M. I. Biggerstaff, and W. D. Rust (2009), Relationships between lightning location and polarimetric radar signatures in a small mesoscale convective system, *Mon. Weather Rev.*, *137*, 4151–4170, doi:10.1175/2009MWR2860.1.
- Martin, R. V., D. J. Jacob, K. Chance, T. P. Kurosu, P. I. Palmer, and M. J. Evans (2003), Global inventory of nitrogen oxide emissions constrained by space-based observations of NO₂ columns, *J. Geophys. Res.*, *108*(D17), 4537, doi:10.1029/2003JD003453.
- Menzel, W. P., and J. F. W. Purdom (1994), Introducing GOES-I: The first of a new generation of geostationary operational environmental satellites, *Bull. Am. Meteorol. Soc.*, *75*, 757–781.
- Nault, B. A., C. Garland, S. E. Pusede, P. J. Wooldridge, K. Ullmann, S. R. Hall, and R. C. Cohen (2015), Measurements of CH₃O₂NO₂ in the upper troposphere, *Atmos. Meas. Tech.*, *8*, 987–997, doi:10.5194/amt-8-987-2015.
- Noxon, J. F. (1976), Atmospheric nitrogen fixation by lightning, *Geophys. Res. Lett.*, *3*, 463–465.
- Ott, L. E., K. E. Pickering, G. L. Stenchikov, D. J. Allen, A. J. DeCaria, B. Ridley, R.-F. Lin, S. Lang, and W.-K. Tao (2010), Production of lightning NO and its vertical distribution calculated from three-dimensional cloud-scale chemical transport model simulations, *J. Geophys. Res.*, *115*, D04301, doi:10.1029/2009JD011880.
- Pan, L. L., et al. (2014), Thunderstorms enhance tropospheric ozone by wrapping and shedding stratospheric air, *Geophys. Res. Lett.*, *41*, 7785–7790, doi:10.1002/2014GL061921.
- Parrish, D. D., et al. (2004), Fraction and composition of NO_y transported in air masses lofted from the North American continental boundary layer, *J. Geophys. Res.*, *109*, D09302, doi:10.1029/2003JD004226.
- Pickering, K. E., Y. Wang, W.-K. Tao, C. Price, and J.-F. Müller (1998), Vertical distributions of lightning NO_x for use in regional and global chemical transport models, *J. Geophys. Res.*, *103*, 31,203–31,216, doi:10.1029/98JD02651.
- Pollack, I. B., B. M. Lerner, and T. B. Ryerson (2011), Evaluation of ultraviolet light-emitting diodes for detection of atmospheric NO₂ by photolysis-chemiluminescence, *J. Atmos. Chem.*, *65*(2), 111–125, doi:10.1007/s10874-011-9184-3.
- Press, W. H., S. A. Teukolsky, W. T. Vetterling, and B. P. Flannery (1988), *Numerical Recipes in C*, Cambridge Univ. Press, Cambridge, U. K.
- Price, C., J. Penner, and M. Prather (1997a), NO_x from lightning. 1. Global distribution based on lightning physics, *J. Geophys. Res.*, *102*, 5929–5941, doi:10.1029/96JD03504.
- Price, C., J. Penner, and M. Prather (1997b), NO_x from lightning. 2. Constraints from the global atmospheric electric circuit, *J. Geophys. Res.*, *102*, 5943–5951, doi:10.1029/96JD02551.
- Reis, S., R. W. Pinder, M. Zhang, G. Lijie, and M. A. Sutton (2009), Reactive nitrogen in atmospheric emission inventories, *Atmos. Chem. Phys.*, *9*(19), 7657–7677, doi:10.5194/acp-9-7657-2009.
- Ridley, B., et al. (2004), Florida thunderstorms: A faucet of reactive nitrogen to the upper troposphere, *J. Geophys. Res.*, *109*, D17305, doi:10.1029/2004JD004769.
- Ridley, B. A., and F. E. Grahek (1990), A small, low flow, high-sensitivity reaction vessel for no chemiluminescence detectors, *J. Atmos. Oceanic Technol.*, *7*(2), 307–311.
- Ridley, B. A., F. E. Grahek, and J. G. Walega (1992), A small, high-sensitivity, medium-response ozone detector suitable for measurements from light aircraft, *J. Atmos. Oceanic Technol.*, *9*(2), 142–148.
- Ridley, B. A., J. E. Dye, J. G. Walega, J. Zheng, F. E. Grahek, and W. Rison (1996), On the production of active nitrogen by thunderstorms over New Mexico, *J. Geophys. Res.*, *101*, 20,985–21,005, doi:10.1029/96JD01706.
- Ridley, B. A., K. E. Pickering, and J. E. Dye (2005), Comments on the parameterization of lightning-produced NO in global chemistry-transport models, *Atmos. Environ.*, *39*(33), 6184–6187, doi:10.1016/j.atmosenv.2005.06.054.
- Rison, W., R. J. Thomas, P. R. Krehbiel, T. Hamlin, and J. Harlin (1999), A GPS-based three-dimensional lightning mapping system: Initial observations in central New Mexico, *Geophys. Res. Lett.*, *26*, 3573–3576, doi:10.1029/1999GL010856.
- Rutledge, S. A., and D. R. MacGorman (1988), Cloud-to-ground lightning activity in the 10–11 June 1985 convective system observed during the Oklahoma-Kansas PRE-STORM project, *Mon. Weather Rev.*, *116*, 1393–1408.
- Ryerson, T. B., et al. (1998), Emissions lifetimes and ozone formation in power plant plumes, *J. Geophys. Res.*, *103*, 22,569–22,583.
- Ryerson, T. B., L. G. Huey, K. Knapp, J. A. Neuman, D. D. Parrish, D. T. Sueper, and F. C. Fehsenfeld (1999), Design and initial characterization of an inlet for gas-phase NO_y measurements from aircraft, *J. Geophys. Res.*, *104*, 5483–5492.
- Ryerson, T. B., E. J. Williams, and F. C. Fehsenfeld (2000), An efficient photolysis system for fast-response NO₂ measurements, *J. Geophys. Res.*, *105*, 26,447–26,461.
- Sachse, G. W., J. E. Collins, G. F. Hill, L. O. Wade, L. G. Burney, and J. A. Ritter (1991), Airborne tunable diode-laser sensor for high-precision concentration and flux measurements of carbon-monoxide and methane, *Proc. SPIE*, *1433*, 157–166.

- Schumann, U., and H. Huntrieser (2007), The global lightning-induced nitrogen oxides source, *Atmos. Chem. Phys.*, *7*(14), 3823–3907, doi:10.5194/acp-7-3823-2007.
- Seinfeld, J. H., and S. N. Pandis (2006), *Atmospheric Chemistry and Physics: From Air Pollution to Climate Change*, 2nd ed., Wiley-Interscience, New York.
- Skamarock, W. C., J. G. Powers, M. Barth, J. E. Dye, T. Matejka, D. Bartels, K. Baumann, J. Stith, D. D. Parrish, and G. Hubler (2000), Numerical simulations of the July 10 Stratospheric-Tropospheric Experiment: Radiation, Aerosols, and Ozone/Deep Convection Experiment convective system: Kinematics and transport, *J. Geophys. Res.*, *105*(D15), 19,973–19,990, doi:10.1029/2000JD900179.
- Skamarock, W. C., J. E. Dye, E. Defer, M. C. Barth, J. L. Stith, B. A. Ridley, and K. Baumann (2003), Observational- and modeling-based budget of lightning-produced NO_x in a continental thunderstorm, *J. Geophys. Res.*, *108*(D10), 4305, doi:10.1029/2002JD002163.
- Stark, M. S., J. T. H. Harrison, and C. Anastasi (1996), Formation of nitrogen oxides by electrical discharges and implications for atmospheric lightning, *J. Geophys. Res.*, *101*, 6963–6969, doi:10.1029/95JD03008.
- Stith, J., J. Dye, B. Ridley, P. Laroche, E. Defer, K. Baumann, G. Hübler, R. Zerr, and M. Venticinque (1999), NO signatures from lightning flashes, *J. Geophys. Res.*, *104*, 16,081–16,089, doi:10.1029/1999JD900174.
- Stohl, A., M. Trainer, T. B. Ryerson, J. S. Holloway, and D. D. Parrish (2002), Export of NO_y from the North American boundary layer during 1996 and 1997 North Atlantic Regional Experiments, *J. Geophys. Res.*, *107*(D11), 4131, doi:10.1029/2001JD000519.
- Taylor, J. R. (1997), *An Introduction to Error Analysis: The Study of Uncertainties in Physical Measurements*, 2nd ed., Univ. Sci. Books, Sausalito, Calif.
- Thornton, J. A., P. J. Wooldridge, and R. C. Cohen (2000), Atmospheric NO_2 : In situ laser-induced fluorescence detection at parts per trillion mixing ratios, *Anal. Chem.*, *72*(3), 528–539, doi:10.1021/ac9908905.
- Wang, Y., A. W. DeSilva, G. C. Goldenbaum, and R. R. Dickerson (1998), Nitric oxide production by simulated lightning: Dependence on current, energy, and pressure, *J. Geophys. Res.*, *103*, 19,149–19,159, doi:10.1029/98JD01356.
- Ziereis, H., H. Schlager, P. Schulte, P. F. J. van Velthoven, and F. Slemr (2000), Distributions of NO , NO_x , and NO_y in the upper troposphere and lower stratosphere between 28° and 61°N during POLINAT 2, *J. Geophys. Res.*, *105*, 3653–3664, doi:10.1029/1999JD900870.